LITTLE THINGS

Deidre A. Hunter[1], Dana Ficut-Vicas[2], Trisha Ashley[3], Elias Brinks[2], Phil Cigan[4], Bruce G. Elmegreen[5], Volker Heesen[2,6], Kimberly A. Herrmann[1,7], Megan Johnson[1,8,9], Se-Heon Oh[10,11], Michael P. Rupen[12], Andreas Schruba[13,14], Caroline E. Simpson[3], Fabian Walter[13], David J. Westpfahl[4], Lisa M. Young[4], and Hong-Xin Zhang[1,15,16]

ABSTRACT

We present LITTLE THINGS (Local Irregulars That Trace Luminosity Extremes, The H I Nearby Galaxy Survey) that is aimed at determining what drives

[1]Lowell Observatory, 1400 West Mars Hill Road, Flagstaff, Arizona 86001 USA

[2]Centre for Astrophysics Research, University of Hertfordshire, College Lane, Hatfield, AL10 9AB United Kingdom

[3]Department of Physics, Florida International University, CP 204, 11200 SW 8th St, Miami, Florida 33199 USA

[4]Physics Department, New Mexico Institute of Mining and Technology, Socorro, New Mexico 87801 USA

[5]IBM T. J. Watson Research Center, PO Box 218, Yorktown Heights, New York 10598 USA

[6]Current address: School of Physics and Astronomy, University of Southampton, Southampton SO17 1BJ UK

[7]Current address: Department of Physics, Pennsylvania State University Mont Alto, Science Technology Building, Mont Alto, PA 17237 USA

[8]Department of Physics and Astronomy, Georgia State University, 29 Peachtree Center Avenue, Science Annex, Suite 400, Atlanta, Georgia 30303-4106 USA

[9]Current address: National Radio Astronomy Observatory, PO Box 2, Green Bank, WV 24944-0002 USA

[10]The International Centre for Radio Astronomy Research (ICRAR), The University of Western Australia, 35 Stirling Highway, Crawley, Western Australia 6009, Australia

[11]ARC Centre of Excellence for All-sky Astrophysics (CAASTRO)

[12]National Radio Astronomy Observatory, 1003 Lopezville Road, Socorro, NM 87801 USA

[13]Max-Planck-Institut für Astronomie, Königstuhl 17, 69117 Heidelberg Germany

[14]Current address: Center for Astronomy and Astrophysics, California Institute of Technology, 1200 E California Blvd, MC 249-17, Pasadena, CA 91125, USA

[15]Purple Mountain Observatory, Chinese Academy of Sciences, 2 West Beijing Road, Nanjing 210008 P. R. China

[16]Current address: Peking University, Astronomy Department, No. 5 Yiheyuan Road, Haidian District, Beijing, P. R. China 100871

star formation in dwarf galaxies. This is a multi-wavelength survey of 37 Dwarf Irregular and 4 Blue Compact Dwarf galaxies that is centered around H I-line data obtained with the National Radio Astronomy Observatory (NRAO) Very Large Array (VLA). The H I-line data are characterized by high sensitivity (≤ 1.1 mJy beam^{-1} per channel), high spectral resolution (≤ 2.6 km s^{-1}), and high angular resolution ($\sim 6''$). The LITTLE THINGS sample contains dwarf galaxies that are relatively nearby (≤ 10.3 Mpc; $6''$ is ≤ 300 pc), that were known to contain atomic hydrogen, the fuel for star formation, and that cover a large range in dwarf galactic properties. We describe our VLA data acquisition, calibration, and mapping procedures, as well as H I map characteristics, and show channel maps, moment maps, velocity-flux profiles, and surface gas density profiles. In addition to the H I data we have *GALEX* UV and ground-based *UBV* and Hα images for most of the galaxies, and *JHK* images for some. *Spitzer* mid-IR images are available for many of the galaxies as well. These data sets are available on-line.

Subject headings: galaxies: irregular — galaxies: star formation — galaxies: ISM — galaxies: kinematics and dynamics — galaxies:structure

1. Introduction

Dwarf Irregular (dIrr) galaxies are the most common type of galaxy in the local universe (see, for example, Dale et al. 2009). They are also the closest analogs to the low mass dark matter halos that formed after the Big Bang. In the ΛCDM model, it is in these entities that the first stars formed. Yet, we do not understand what drives star formation on galactic scales even in nearby dwarfs, the simplest, most pristine local environments (see, for example, Hunter 2008, Bigiel et al. 2010). To remedy this situation we have assembled multi-wavelength data on a large sample of relatively normal, nearby gas-rich dwarf galaxies, tracing their stellar populations, gas content, dynamics, and star formation indicators. This project is called LITTLE THINGS (Local Irregulars That Trace Luminosity Extremes, The H I Nearby Galaxy Survey), and it builds on the THINGS project, whose emphasis was on nearby spirals (Walter et al. 2008).

LITTLE THINGS[17] was granted ~ 376 hours with the Very Large Array (VLA[18]) in B,

---

[17] http://www.lowell.edu/users/dah/littlethings/index.html

[18] The VLA is a facility of the National Radio Astronomy Observatory (NRAO). The NRAO is a facility

C, and D configurations to obtain H I-line data of 21 dIrr and Blue Compact Dwarf (BCD) galaxies. We added another 20 galaxies from the VLA archives for a total sample of 37 dIrr and 4 BCD galaxies covering a large range of dwarf galactic parameter space. Our VLA data emphasize deep, high spatial (6″) and spectral (≤ 2.6 km s^{-1}) resolution in order to reveal clouds, shells, and turbulence in the interstellar medium (ISM) that could be important for creating regions of higher density star-forming gas. We are combining the H I-line data with ultraviolet (UV), optical, and infrared (IR) data to address the following questions:

What regulates star formation in small, gas-rich galaxies? Studies of the star formation laws in galaxies show that star formation is very inefficient in dwarf galaxies and in the outer disks of spirals (Bigiel et al. 2010; Ficut-Vicas et al., in preparation). Furthermore, the star formation efficiency decreases as the gas density decreases. How then do atomic hydrogen clouds form in the low gas density environments of dwarfs that ultimately lead to star-forming molecular clouds?

What is the relative importance of sequential triggering by previous generations of stars for star formation in dwarf galaxies? One generation of stars can trigger the formation of the next by rearranging the gas through winds and supernova explosions (see, for example, Öpik 1953, Gerola et al. 1980, Comins 1983, Dopita et al. 1985, Mori et al.1997, van Dyk et al. 1998), but how important is this process? Observations of dwarfs show a better correlation between the star formation rate and the V-band surface brightness, which emphasizes Gyr old stars, than with any other measure, including the average gas density (Hunter et al. 1998). Does this relationship imply a significant causal relationship in which existing stars are important for triggering new star formation?

What is the relative importance of random turbulent compression cloud formation in dwarf galaxies? Turbulence can account for a wide range of phenomena that are indirectly related to star formation: the power law luminosity functions of H II regions, the power law mass functions of clouds and clusters (Mac Low & Klessen 2004), the shape of the power spectra of H I (Stanimirović et al. 1999, Elmegreen et al. 2001, Dickey et al. 2001, Zhang et al. 2012a) and Hα (Willett et al. 2005), the log-normal distribution of the Hα intensity in individual pixels in Hα images of dwarf galaxies, (Hunter & Elmegreen 2004), the correlation between region size and the star formation time scale (Efremov & Elmegreen 1998), and hierarchical structures in the ISM (Bastian et al. 2007). But how important is

---

turbulence in the formation of star-forming clouds, particularly in the realm of sub-critical gas density?

What happens to the star formation process in the outer parts of disks? We find that many dwarfs have exponential stellar surface brightness profiles with a break and a change in slope. These breaks are similar to what are seen in the outer parts of spirals (e.g., de Grijs et al. 2001; Kregel et al. 2002; Pohlen et al. 2002; Kregel & van der Kruit 2004; Pohlen & Trujillo 2006; Erwin et al. 2008; Gutiérrez et al. 2011) and disks at high redshift (Pérez 2004). The break could imply a change in the star formation process at the break radius, but what is really happening there?

Here we describe the LITTLE THINGS project and present the H I data. Science papers that are part of this project include: 1) "Velocity Dispersions and Star Formation Rates in the LITTLE THINGS Dwarf Galaxies (Cigan et al., in preparation), 2) "Star Formation Laws in LITTLE THINGS Dwarfs: The case of DDO 133 and DDO 168" (Ficut-Vicas et al., in preparation), 3) "Deep Radio Continuum Imaging of the Dwarf Irregular Galaxy IC 10: Tracing Star Formation and Magnetic Fields" (Heesen et al. 2011), 4) "Deep Radio Continuum Observations of the Nearby Dwarf Irregular Galaxy IC 10. I. Nature of the Radio Continuum Emission" (Heesen et al., in preparation), 5) "Surface Brightness Profiles of Dwarf Galaxies. I. Profiles and Statistics" (Herrmann et al. 2012), 6) "Surface Brightness Profiles of Dwarf Galaxies. II. Color Trends and Mass Profiles" (Herrmann et al., in preparation), 7) "The Stellar and Gas Kinematics of the LITTLE THINGS Dwarf Irregular Galaxy NGC 1569" (Johnson et al. 2012), 8) "The Stellar Kinematics of the LITTLE THINGS Dwarf Irregular Galaxies DDO 46 and DDO 168" (Johnson et al., in preparation), 9) "Deep 6 cm Radio Continuum Observations of the Nearby Dwarf Irregular Galaxy IC 1613" (Kitchener et al., in preparation), 10) "High-resolution Mass Models of Dwarf Galaxies from LITTLE THINGS" (Oh et al., in preparation), 11) "Star Formation in IC 1613" (Simpson et al., in preparation), 12) "Outside-in Shrinking of the Star-forming Disk of Dwarf Irregular Galaxies" (Zhang et al. 2012b), and 13) "H I Power Spectrum Analysis of Dwarf Irregular Galaxies" (Zhang et al. 2012a). Other science that is in progress includes, but is not limited to, studies of the following: 1) Star Formation Processes in Blue Compact Dwarfs – Ashley, 2) Molecular Cloud Structure and Dust at Low Metallicity – Cigan, 3) Star Formation Laws of the full sample of galaxies – Ficut-Vicas, 4) Surface Brightness Profiles and their relationship to H I gas and two dimensional images – Herrmann, 5) The Role of Turbulence in Star Formation in Dwarfs – Hunter, 6) A Deep 6 cm Radio Continuum Survey of LITTLE THINGS – Kitchener, and 7) Porosity of the Interstellar Medium in Dwarfs – Simpson.

2. The Survey

2.1. Sample selection

The LITTLE THINGS sample of 37 dIrr galaxies and 4 BCDs was drawn from a larger multi-wavelength survey of 94 relatively nearby dIrr galaxies and 24 BCD systems, as well as 18 Sm galaxies (Hunter & Elmegreen 2004, 2006). A large sample is necessary to disentangle complex processes in surprisingly complicated galaxies. This larger sample covers nearly the full range of galactic parameters seen in dwarf galaxies including luminosity (9 magnitudes in absolute magnitude M_V), current star formation rate normalized to the area within one disk scale length (a range of a factor of 10^4), relative gas content (a factor of 110 in M_{HI}/L_B), and central surface brightness (7 magnitudes in μ_0^V, the central V-band surface brightness). The sample does not include obviously interacting galaxies because we are investigating internal processes, and it only includes dwarfs with substantial amounts of atomic hydrogen so that they *could* be forming stars.

For LITTLE THINGS, we excluded galaxies with distances >10 Mpc in order to achieve a reasonably small spatial resolution in the VLA H I maps (<300 pc at 10 Mpc in B array), although the distance to our most distant galaxy was revised later to 10.3 Mpc. The average distance to the galaxies in our sample is 3.7 Mpc. In addition we excluded galaxies with W_{20} >160 km s^{-1} in order to fit the galaxy emission comfortably in the bandwidth available for our desired velocity resolution, leaving room for determining continuum emission. The parameter W_{20} is the full-width at 20% of the peak of an integrated H I flux-velocity profile (Bottinelli et al. 1990). One galaxy originally in our sample, NGC 1156, was eliminated when we discovered that the archival data contained no line-free channels. We also excluded galaxies with high inclinations (>70°) so that we can better resolve structures in the disks. We then insisted that the LITTLE THINGS sample cover the range of integrated properties seen in the full optical survey, especially M_V and star formation rate, including galaxies without any measurable Hα emission. A comparison of the properties of the LITTLE THINGS sample with the larger parent sample is shown in Figure 1. Our sample includes 19 dIrr galaxies and one BCD galaxy in the VLA archives having B/C/D-array observations at 2.6 km s^{-1} channel separation or better. Our new VLA observations are of 18 dIrr galaxies and 3 BCDs in the B/C/D arrays. In total, 19 galaxies have H I-line data at 1.3 km s^{-1} channel separation.

One of our 41 galaxies, NGC 6822, which we observed at 1.3 km s^{-1} channel separation, is highly extended compared to the primary beam. Those data require special treatment and calibration and mapping are in progress. Below, we list the data we obtained on NGC 6822, but we do not include it in the discussions of the H I maps and cubes.

Table 1 lists the sample galaxies and several basic properties, including other names by which the galaxies are known, distances, M_V, a measure of size, foreground reddening, star formation rates, and oxygen abundance. Here we elaborate on a few of the quantities: 1) Distance. In choosing a distance for each galaxy, we considered the references for distance determinations given by the NASA/IPAC Extragalactic Database (NED). In order of preference, we chose distances determined from Cepheids or RR Lyrae stars and from the tip of the red giant branch. The references for the distance used for each galaxy are given in Table 1. If none of those determinations was available, we used the Hubble flow distance determined from the galaxy's radial velocity corrected for infall to the Virgo Cluster (Mould et al. 2000) and a Hubble constant of 73 km s^{-1} Mpc^{-1}. 2) Size measurement. For a measure of the size of the galaxy, we used the Holmberg radius, R_H, which was originally measured by Holmberg (1958) at a photographic surface brightness of 26.5 mag in 1 arcsec^2. Here we have used the R_H measured by Hunter & Elmegreen (2006), who converted from photographic magnitudes to B-band magnitudes using the recipe of de Vaucouleurs et al. (1976). For our galaxies this corresponds to a B-band surface brightness of between 26.60 and 26.72 mag in 1 arcsec^2 with an average of 26.64±0.002 mag in 1 arcsec^2. 3) Star formation rate (SFR). Star formation rates are taken from Hunter & Elmegreen (2004). These were determined from integrated Hα luminosities and are normalized to the area encompassed by one disk scale length. We use this characteristic area to normalize the SFRs in order to compare galaxies of different size, but this is not the area that encompasses Hα emission. Some galaxies have Hα emission that extends less than and others more than one disk scale length. 4) Oxygen abundances. As a measure of the metallicity of the galaxy we list oxygen abundances, $12+\log O/H$, taken from the literature and determined from H II regions. For galaxies without H II region abundance measurements, we used M_B and the luminosity-metallicity relationship of Richer & McCall (1995). The abundance determined this way, listed in parentheses, is very uncertain, but it gives an indication of the expected relative metallicity of the galaxy. The references for the abundances are given in the Table. For comparison the solar oxygen abundance value is 8.69 (Asplund et al. 2009).

2.2. VLA observational philosophy

Our new VLA observations are characterized by deep observations with high angular and high spectral resolution. To achieve the angular resolution and sensitivity we needed, we used VLA B/C/D-array configurations with 12/6/2 hr integration times per galaxy. The combined B/C/D arrays sample the galaxies at 6″ (110 pc at 3.7 Mpc, the average distance of our sample; for ROBUST-weighting). This resolution shows clouds, shells, and turbulent structures that are important for star formation. The B array, which is the most extended

configuration of the three we used, requires the most time because of its reduced surface brightness sensitivity, but the high resolution it provides is essential. Typical clouds and holes are of order 100 pc in diameter, and they would be lost at the resolution of the data obtained in the more compact C and D arrays (the resolution of C+D is $\sim 20''$, or 360 pc at 3.7 Mpc). However, the C and D arrays are important because they reveal the extended, low-density gas around clouds, shells, and star formation. Low spatial resolution maps also trace the low density H I far beyond the stellar disks. The D array can detect structure up to a scale of $15'$.

For good velocity resolution, we chose a channel separation of 1.3 km s^{-1} and 2.6 km s^{-1}, both for new observations and for data we drew from the archives. The choice of channel separation was dictated by the need to contain galaxy emission within the bandwidth, leaving line-free channels on either side for continuum subtraction. Twenty-two galaxies have only Hanning-smoothed data cubes with 2.6 km s^{-1} channel separation, and 19 have small enough velocity ranges to be observed and imaged with 1.3 km s^{-1} channel separation. These relatively small channel separations enable the resolution of kinematic structures in the galaxies, especially the deconvolution of warm and cool components with velocity FWHM as small as 7-9 km s^{-1}(Young et al. 2003).

In our sample of galaxies requiring new VLA observations, 13 had no previous VLA observations, and 8 had some data in the archives. Altogether, there were 21 galaxies that needed B array observations, 15 that needed C, and 17 needed D configurations. Seven of our galaxies are part of the VLA-ANGST (ACS [Advanced Camera for Surveys] Nearby Galaxy Survey Treasury) large project (Ott et al. 2010; project ID AO215) that began at the same time as LITTLE THINGS: CVnIdwA, DDO 70, DDO 75, DDO 155, DDO 187, NGC 4163, UGC 8508. The VLA-ANGST integration times were generally shallower than those of LITTLE THINGS, but these galaxies were observed as part of VLA-ANGST rather than LITTLE THINGS and we use those data here. In addition eight of our galaxies taken entirely from the archives were part of the THINGS (Walter et al. 2008) sample (DDO 50, DDO 53, DDO 63, DDO 154, M81dwA, NGC 1569, NGC 2366, NGC 4214). For the THINGS galaxies, we retrieved their uv-calibrated data.

There are two galaxies that are exceptions to our combination of the B/C/D array configurations. These galaxies are DDO 216 and SagDIG. The data for these galaxies were taken from the archives where only C and D array configuration data were available.

2.3. Ancillary data

We also have a rich multi-wavelength collection of ancillary data on the LITTLE THINGS galaxies. Our data sets are summarized in Table 2. We have two tracers of the products of recent star formation. First, Hα images obtained at Lowell Observatory reveal the presence of massive stars formed over the past 10 Myrs through the ionized nebulae of their natal clouds (Hunter & Elmegreen 2004). Second, ultraviolet images at 1516 Å and 2267 Å obtained with the *Galaxy Evolution Explorer* satellite (*GALEX*; Martin et al. 2005) show the bright ultraviolet starlight from stars formed over the past 100–200 Myrs (Hunter et al. 2010). The ultraviolet images are a more reliable tracer of recent star formation especially in the outer disks of galaxies where star formation is more sporadic and lower gas densities make H II regions harder to detect. The *GALEX* data were processed with the GR4/5 pipeline.

Older stars are traced with UBV images obtained at Lowell Observatory (Hunter & Elmegreen 2006). For on-going star formation, these are sensitive to stars formed over the past 1 Gyr. For 17 of the galaxies, we also have some combination of JHK images obtained at Lowell Observatory, and for 36 galaxies there are *Spitzer* 3.6 μm images that we have pulled from the archives. The near and mid-IR images in particular highlight the star formation activity integrated over a galaxy's lifetime.

Dust plays an important, although poorly understood, role in the star formation process. FIR continuum emission traces this part of the ISM. *Spitzer* 5.8 μm and 8.0 μm images trace polycyclic aromatic hydrocarbon (PAH) emission (plus hot dust continuum emission). *Spitzer* MIPS images of 35 of the galaxies, obtained as part of the *Spitzer* Infrared Nearby Galaxies Survey (SINGS), Local Volume Legacy (LVL), and other programs, can in principle give the dust continuum emission and distribution at 24 μm, 70 μm, and 160 μm, although exposures tend to be shallow. We are also mapping a subset of galaxies in the FIR with bolometer arrays on the Atacama Pathfinder EXperiment (APEX) sub-millimeter telescope in collaboration with M. Rubio and with *Herschel* (Pilbratt et al. 2010; an OT2, priority 1 program) in collaboration with S. Madden. These data are important for understanding the heating balance in the ISM.

Molecular clouds are a key component of the ISM and the component most directly connected with star formation. We are exploring this part of the star formation process through case studies. This has included Combined Array for Research in Millimeter-wave Astronomy (CARMA) observations of CO line emission in NGC 3738, a dwarf with intense star formation in the center of the galaxy. With APEX we mapped CO in WLM, a typical star-forming dwarf, in collaboration with M. Rubio. We are also using *Herschel* (an OT1, priority 1 program) to map photo-dissociation regions (PDRs) in five of the LITTLE

THINGS galaxies in collaboration with M. Kaufman and S. Madden. These data will allow us to characterize molecular clouds at low metallicity.

3. VLA observations and data reduction

3.1. Observing

The LITTLE THINGS (project AH927) observations began with the B-array 2007 December 19 and, for B-array, ended 2008 February 10. The observations were done in two 6-hour segments for each galaxy. Some observations were repeated when technical hiccups occurred. C-array observations followed in the spring of 2008, and D-array observations in the summer of 2008. All of our new observations were in hand by the beginning of August 2008. The observations are listed in Table 3. Each array configuration with which a galaxy was observed is listed separately. Multiple observing sessions for each configuration are identified by the dates on which the observing sessions began.

Our new observations used a bandwidth of 0.8 or 1.6 MHz (nominally 150 and 300 km s^{-1} wide), depending on the known velocity range of emission from each galaxy. We used two intermediate frequencies (IFs; 2AC) and 256 channels.

Our new data were not Hanning smoothed when the observations were made. Thus, the galaxies for which we were targeting a spectral resolution of 2.6 km s^{-1} (12.21 kHz) were observed with a channel separation of 1.3 km s^{-1} (the spectral resolution is 1.4 times this), and in the reduction stage the data were Hanning-smoothed to obtain a channel separation and resolution of 2.6 km s^{-1}. Similarly, galaxies for which we targeted a spectral resolution of 1.3 km s^{-1} (6.10 kHz) were observed with a channel separation of 0.65 km s^{-1} (3.05 kHz) and later Hanning-smoothed to obtain a channel separation and resolution of 1.3 km s^{-1}. Most of the data from the archives were on-line Hanning smoothed. The exception is SagDIG, which was observed with a channel separation of 3.05 kHz and no Hanning-smoothing. For that galaxy, we produced a cube with the native resolution (1.4× the channel separation of 0.65 km s^{-1}), and another cube with Hanning smoothing to produce a channel separation and resolution of 1.3 km s^{-1}.

Because of the transition of the VLA to EVLA during the course of the survey, sensitivity changes, phase drifts, and phase jumps were expected. To deal with this required that careful calibration be built into the observations. Our observations in general began and ended with a primary flux calibrator, usually 3C286, allowing extra time at the beginning in case of a cable wrap problem in moving to our galaxy position. It was also recommended to add a short dummy scan to make sure the antennas were properly initialized at the be-

ginning of the observing session. The primary calibrator was used to set the flux scale and for determining the response function across the bandpass. In between these observations we alternated between the secondary calibrator and the galaxy with approximately 12-25 minutes on source at any one time. The shorter on-source dwell times were in the shorter observing sessions. Because of our narrow bandwidth, when offered with a choice, we preferred a strong calibrator, even if it was at a radial distance that was larger than that of a more nearby, but weaker one. This was possible because of the phase stability of the VLA at 20 cm even in the B-configuration. Even so, the secondary calibrators were always within about 12° of a target galaxy. The secondary calibrator was used to determine the variations of phase and amplitude with time during the observing session. The time spent on source in each configuration is given in Table 3.

3.1.1. The Aliasing Problem

During the course of our observations, the VLA was in transition to the EVLA, and antennas were being outfitted with new receivers and electronics one by one. At the beginning of our observations 46% of the antennas in the array had been converted, and by the end 62% of the array consisted of EVLA antennas. To make the digital signal from EVLA antennas compatible with the old analog VLA correlator, the signal on the new receivers was passed through an electronic filter. However, this conversion caused power from sidebands to be aliased into the lower 700 kHz of the observing bandwidth (the "aliasing problem" [15]). In spectral line mode, the line emission would be unaffected as long as the bandwidth used was at least 1.5 MHz and the spectral line observed was narrow enough so that it fell beyond the affected 0.7 MHz or the line could be shifted away from the band center. However, even so, continuum emission was aliased, with phase information scrambled making it resemble noise, the effect being strongest in channels closest to the baseband edge. This is most noticeable on EVLA-EVLA baselines, and to a lesser extent on EVLA-VLA baselines; VLA-VLA baselines were not affected (see Figure 2).

This problem had a serious impact on LITTLE THINGS, which used narrow bandwidths. A key element of our project is high spectral resolution imaging at high sensitivity of these faint, low rotation velocity objects. Thus, our galaxies were being observed with small bandwidths (0.78 MHz or 1.56 MHz) in order to achieve high spectral resolution (1.3 km s^{-1} or 2.6 km s^{-1}). We examined our data to understand the consequences of the aliasing problem and how we might deal with it. We took 1.56 MHz bandwidth data of

---

[15]http://www.vla.nrao.edu/astro/guides/evlareturn/aliasing.shtml/

one of our galaxies and fully calibrated and mapped it, running extensive tests. We clearly saw increased noise from the lower band edge to the middle of the passband when EVLA-EVLA and VLA-EVLA baselines were included (Figure 2). In the end, we were able to satisfactorily calibrate the data only by eliminating the EVLA-EVLA baselines. Subtracting the continuum from the line data using a fourth order polynomial, as had originally been suggested, resulted in unacceptable amplitude variations across the bandpass. An alternative scheme using unaffected baselines to gauge the level of the continuum worked at some level, but continuum remained in the map at unpredictable levels. Furthermore, the noise added to the overall dataset by the EVLA-EVLA baselines was at such an extent that the noise in a data set containing all baselines and the noise in the same data set without EVLA-EVLA baselines are at virtually the same level. This means that, even if it were possible to calibrate properly the EVLA-EVLA baselines, this would not reduce the noise level.

Because the EVLA-EVLA baselines constituted 22% of the total in B-array, we requested a 22% increase in our B-array observing time, or 55.5 hours, in order to make up for the lost EVLA-EVLA baselines and achieve our original target signal-to-noise. This was granted in the form of dynamically scheduled time, in blocks of 1–2 observing sessions (2.5–3 hr) per galaxy. Similarly, time for C and D array observations were increased in proportion to the percentage of EVLA-EVLA baselines lost, and this extra time was dynamically scheduled as well. A consequence of the dynamic scheduling was that some of the make-up time came during array configuration transitions and not when the instrument was in a "pure" configuration (see Table 3).

We were worried that the loss of the EVLA-EVLA baselines might change the uv-coverage that we expected. Comparing the uv-coverage with and without EVLA-EVLA baselines removed, however, showed that the antennas were being retrofitted in a pattern that affected the uv-coverage only slightly and caused sidelobe structure that could be dealt with in the imaging stage by employing a suitable CLEAN algorithm (see Appendix B).

3.1.2. Doppler Tracking

Another consequence of the VLA-EVLA transition was that Doppler tracking was not possible. Because the LO chains for EVLA and VLA front-ends are different, frequency changes can cause phase jumps between EVLA and VLA antennas. Therefore, observing at a fixed frequency was recommended. This meant that the frequency of the observations changed by small amounts during the course of an observing session. We chose our central frequency for the expected date and time of the observations, and checked to ensure that the galaxy would not move out of the channel during the observations. Trickier were the

dynamically scheduled observations. For those, we chose a date in the middle of the range of possible observation dates. In no case did the galaxy emission move out of the channels, but this added an additional concern in setting up the observe files and an additional step in mapping the data.

3.1.3. Avoiding Milky Way Emission

Another problem arose for six galaxies with radial velocities that are similar to those of H I in the Milky Way in the direction of the galaxy, potentially leading to Milky Way emission in the passband. These galaxies include DDO 165, DDO 167, DDO 187, NGC 4163, NGC 6822, and UGC 8508. (NGC 1569 was observed before the transition to EVLA as part of THINGS.) The standard approach in these cases is to observe both primary and secondary calibrators at velocities offset from that of Galactic H I in their direction. This is accomplished by applying a frequency offset to a higher and lower central frequency, symmetrically with respect to the originally intended central frequency. The offset needs to be large enough to shift the entire bandwidth beyond the range where Galactic H I is present. However, because phase jumps were expected to accompany frequency shifts with the EVLA antennae, we observed only the primary calibrator with a positive and negative offset, ensuring it was unaffected by Galactic foreground H I. Because no absolute phase calibration is required for the flux and bandpass calibration, the phase jumps accompanying any frequency shifts were irrelevant for the primary calibrator. For NGC 6822, there were two flux calibrators—3C286 and 3C48, and both were offset in frequency. The offset was 3 MHz for 4 of the galaxies, and 3.5 MHz for DDO 187 and 2.5 MHz for NGC 6822.

Unfortunately, in calibrating these data we found a problem with some of the calibrator observations on one side of the central frequency. From discussions with Ken Sowinski at NRAO we realized that this was due to reassignment of the Local Oscillator (LO) settings by the on-line system that tunes the receivers, which meant the frequency range of the incoming signal fell partly beyond the range selected by the front end filter. We, therefore, had to throw out the corrupted observation of the calibrator and use only the frequency offset observation on the side which was not corrupted. This affects the flux calibration at a level of at most 0.1% and can therefore be safely ignored.

3.2. Calibration

The VLA data were calibrated and mapped by many members of the team. Usually one person would calibrate all of the data sets for a galaxy, and similarly one person would usually complete the mapping of a galaxy. As data sets were calibrated or the ensemble of data sets for a galaxy was mapped, the data were uploaded to an internet-accessible hard disk provided and maintained by NRAO, making it available to the rest of the team and the next person who would work on the data. The final map cubes were then examined by designated "checkers" who inspected all of the data, looking for signs of any problems or inconsistencies. A galaxy was not considered "done" until it had passed a thorough inspection, and any and all problems were resolved.

In order to ensure uniform treatment of the data, we created "recipes" for data calibration and mapping that were carefully followed. Since the THINGS survey (Walter et al. 2008) had already been through this process and two of our team members were part of THINGS, we started with their recipe and updated it to reflect changes in software, complications due to the aliasing problem, and problems resulting from the frequency shifts for observations that could be contaminated by Galactic H I. In order to ensure a homogeneous data set, we treated the archival data the same way that we treated the new data. All of the reductions were done in the Astronomical Image Processing System (AIPS) developed by NRAO, version 31DEC08. We used the flux scale of Baars et al. (1977).

We outline the salient calibration steps in Appendix A, and the recipe itself is available on the public web site discussed in §5. After every action on the data, we had at least one, and usually multiple, quality control checks. We outline the salient calibration steps, including those to check the quality of the calibration, in Appendix A. The recipe itself is available on the public web site discussed in §5. For the cases involving multiple frequencies, most steps had to be run for each frequency.

A few circumstances yielded special calibration challenges: 1) Strong winds and many technical problems resulting in phase jumps meant that considerable data had to be eliminated, limiting the data obtained 2008 February 4, affecting DDO 101 (B array). 2) There was a clock error on data taken in B array 2008 January 5 and 7 and only VLA-VLA baselines could be used. The galaxies that were affected were DDO 46, DDO 52, and DDO 133. A similar problem on 2008 January 24 rendered all data from EVLA antennas unusable, affecting DDO 87 and DDO 167. 3) All of the EVLA antennas had to be flagged during the archive 2006 B array observations of VII Zw 403. Four antennas were involved. 4) Solar interference affected the observations in compact configurations of some galaxies, usually those data ≤ 1 kλ: DDO 43 (C and D arrays), DDO 47 (D array), DDO 52 (D array), DDO 87 (C array), F564-V3 (D array), IC 1613 (C and D arrays), NGC 3738 (D array), NGC

4163 (D array), WLM (B and C arrays), and VII Zw 403 (C and D arrays). 5) There were problems with the phases in the right polarization (RR), and some of the left (LL), of the primary phase calibrator of DDO 43 (C array) in the archival data obtained in 2000 April. To deal with this, we performed the bandpass calibration on the secondary instead of the primary calibrator, flagged most of the left polarization data on the primary calibrator, kept only the left polarization in creating the new Channel 0 (an average of the inner 75% of the frequency channels), ran the usual calibration on the primary and secondary calibrators to get the flux of the secondary calibrator, ran the calibration CALIB only on the secondary, and applied the calibration using CLCAL to the new Channel 0 data. 6) There was no model for the primary calibrator 3C295 used with VII Zw 403 in D array in the archival 1997 data. However, the calibrator is not resolved in D array, so we used our observations of the calibrator instead of a model. Similarly, the secondary calibrators for archival observations of IC 1613 and of WLM in B array were spatially resolved. For IC 1613, we used the C array image of the calibrator as a model for calibrating the B array with a maximum limit on the uv range of 15 kλ. For WLM, the effect was small enough to ignore. 7) One galaxy, DDO 101, was self-calibrated in C and D arrays using a 2.3 Jy continuum source in the field. 8) The secondary calibrator, $0925 + 003$, of the archive data on DDO 70 had poor signal-to-noise (flux of $\sim$0.6 Jy). 9) For IC 10, the D array observation that we used is the central pointing (QUAL=13) of a 25-pointing mosaic (Wilcots & Miller 1998).

3.3. Imaging

The mapping recipe picks up where the calibration leaves off, beginning with extracting the calibrated uv-data for just the galaxy from the uv-data set (SPLIT). The individual data sets taken in B, C, and D-configuration, were combined into one large uv-file, ready to be Fourier transformed to create maps in the image plane containing structure across a range of angular scales, from a few arcseconds up to several arcminutes. The spectra from different data sets were aligned in frequency space (CVEL), and the uv-data sets combined (DBCON, with no adjustments to the relative weights). We subtracted continuum emission in the uv-plane (UVLSF), followed by mapping.

The commonly used mapping/CLEAN algorithms for VLA data approximate all emission structure as the sum of point sources. This is clearly an unrealistic approximation for extended galactic emission. In addition, the resulting map is the sum of the clean components that are made with the clean synthesized beam and the residuals that are a product of the dirty beam. So, for mapping, we were excited by the advantages that multi-scale or multi-resolution CLEAN (MS-CLEAN) might bring. This concept, developed by Wakker &

Schwarz (1988), solves simultaneously for point sources and Gaussians with pre-determined sizes (Cornwell 2008). This has been implemented in AIPS under IMAGR by Eric Greisen (Greisen et al. 2009). However, there has been limited experience with using this algorithm in the community (Rich et al. 2008). Therefore, before we could adopt it as our standard, we invested considerable time experimenting with the algorithm in order to understand the consequences to the data, in particular comparing MS-CLEAN maps against those produced with standard CLEANing methods (for more details see Appendix B). We concluded that the MS-CLEAN algorithm gave superior maps and that we understood it well enough to adopt it for making the LITTLE THINGS map cubes. We then finalized our mapping recipe around the AIPS MS-CLEAN option in IMAGR (see details in Appendix B).

We produced both a Natural-weighted image cube, which we expected would bring out extended lower surface brightness emission at the expense of angular resolution and beam profile, and one weighted with a ROBUST value of 0.5 (Briggs 1995), which produces a better behaved synthesized beam at a resolution that is close to that obtained with Uniform-weighting. Usually, the ROBUST-weighted cube was cleaned to 2×rms and the Natural-weighted cube to 2.5×rms. These levels were chosen after extensive tests that showed that the flux that was recovered by MS-CLEAN was not a strong function of CLEAN level, as long as that level was within factors of a few of the optimum level. Cleaning deeper than 2×rms gave noticeable CLEAN artifacts; cleaning down to 3-4×rms left significant residual flux in the different scale maps. We converged on a level of 2×rms. However, the Natural-weighted cubes cleaned to 2×rms showed signs of slight over-cleaning ("holes" dug in the background). For the Natural-weighted cubes we found that 2.5×rms was the best compromise. Each map cube was carefully inspected for signs of over- or under-cleaning.

The maps of two galaxies, Mrk 178 and VII Zw 403, required small tweaks to this scheme. For Mrk 178, our standard CLEAN to 2×rms with the ROBUST-weighting produced a field at the 15″ scale (see Appendix B) that appeared to be over-cleaned. We, therefore, cleaned that scale to 2.5×rms, but the other scales to 2×rms. For VII Zw 403, a CLEAN depth of 2×rms resulted in being able to see the CLEAN box in the first two fields (0″, 15″), and so those limits were raised to 2.5×rms. In both cases, the Naturally-weighted cube with the standard CLEANing depth of 2.5×rms produced good results.

For galaxies with all new data, we produced cubes at the observed spectral resolution and a second set with Hanning-smoothing applied. The Hanning-smoothed version is presented here. For cases where we were combining new data (not Hanning-smoothed) with archival data that were Hanning-smoothed, we shifted the new data in frequency space with the Hanning-smoothing option turned on (CVEL).

To remove the portion of each channel map that was only noise, we used the Natural-

weighted map cube to determine emission from the galaxy. We smoothed the original map cube to a beam of $25'' \times 25''$ (CONVL) and blanked all pixels below 2-2.5rms of the smoothed cube (BLANK). We then made a second pass, blanking by hand any additional emission that was clearly noise (for example, features that do not appear in several consecutive spectral channels). This blanked cube served as the master cube that was used as a conditional transfer for the cubes with smaller beam size. We made flux-weighted moment maps from the resulting data cubes (XMOM): integrated H I, intensity-weighted velocity field, and intensity-weighted velocity dispersion. We corrected the integrated H I map for attenuation by the primary beam (PBCOR) and replaced blanks with values of zero (REMAG).

A few galaxies were affected by Galactic emission. For VII Zw 403 Galactic emission is apparent in the C and D array data. The channels containing Galactic emission but no VII Zw 403 emission were blanked. However, Galactic emission in the channels that contain VII Zw 403 emission was not removed. For NGC 1569 Galactic emission is a serious contaminant over a large velocity range. See Johnson et al. (2012) for a discussion of how that galaxy was handled.

We had particular problems imaging DDO 75. There were 8 uv data sets including AB (when the configuration is in transition from A to B), B, C, and D array configurations. Six of the data sets were archival and two were obtained under project AO 215. The moment maps have low level diagonal striping, and the integrated H I maps have individual blanked pixels ("pinholes") where there should be flux. The increased noise from the striping caused the algorithm that produced the moment maps (XMOM) to calculate unreasonable velocity values, and so those pixels were blanked in the moment map. We tried to identify the cause of the striping, but it appears at such a low level in the uv-data that we could not isolate and remove it. We concluded by cleaning to $3 \times$rms since cleaning to $2 \times$rms looked overcleaned and produced many more pinholes.

Information about the ROBUST-weighted and Natural-weighted map cubes are given in Table 3, along with the channel separation of the observations and the final number of frequency channels in the cube. For each cube we give the beam full-width at half of maximum (FWHM) along the major and minor axes, the beam position angle, and the rms in the maps. The rms in a single channel varies from 0.46 to 1.1 mJy beam^{-1} in our sample. The pixel size of the cubes is $1.5''$, except for DDO 216 and SagDIG, which were observed only in C and D array configurations and were mapped with $3.5''$ pixels because of their significantly larger beam. The map sizes are usually 1024×1024 pixels. A few particularly large galaxies on the sky or galaxies with nearby Galactic emission were imaged at 2048×2048 pixels.

4. Basic Analysis

For each galaxy we have measured the total mass in H I, determined the H I flux-velocity profile, and measured the H I surface density profile. These basic analysis products are presented here. To make these measurements, we used the Groningen Image Processing System (GIPSY, Vogelaar & Terlouw 2001).

The cube channel map units are in Jy beam^{-1}. This is related to brightness temperature in degrees Kelvin through

$$S(\text{Jy beam}^{-1}) = 1.65 \times 10^{-6} \Delta\alpha\Delta\delta \; T_B(K)$$

(Brinks, private communication), where $\Delta\alpha$ and $\Delta\delta$ are the major and minor axis FWHM in arcseconds given in Table 3. The integrated H I map is obtained after converting the channel maps to units of K km s^{-1} using the above relation and summing along the velocity axis. The column density becomes

$$N_{HI}(\text{atoms cm}^{-2}) = 1.823 \times 10^{18} \sum T(\text{K})\Delta V(\text{km s}^{-1}),$$

which becomes

$$N_{HI}(\text{atoms cm}^{-2}) = 1.105 \times 10^{21} S(\text{Jy beam}^{-1} \text{ m s}^{-1})/(\Delta\alpha\Delta\delta)$$

(Hibbard et al. 2001). The H I mass profile is obtained by integrating the flux in each channel map over the area containing H I emission and dividing by the number of pixels per beam area to arrive at S expressed in Jy. The conversion to total mass is then

$$M_{HI}(\text{M}_\odot) = 235.6 \; D(\text{Mpc})^2 \sum S(\text{Jy})\Delta V(\text{km s}^{-1}).$$

The factors for converting fluxes to masses for our ROBUST-weighted integrated H I maps are given in Table 4.

4.1. HI masses

To measure the total H I mass, we summed the flux over the primary-beam corrected integrated H I map made from both the Natural-weighted image cube and the ROBUST-weighted cube (FLUX). Since the integrated H I maps had been constructed from the blanked cubes and pixels without emission had values of zero, the flux was summed over the entire image. The flux was then converted to mass. The masses from the two maps agree well. The average of the absolute value of the differences between the masses measured from the

ROBUST-weighted maps and those measured from the Natural-weighted maps is 11%, with the ROBUST-weighted masses often higher than the Natural-weighted masses.

The fluxes and masses from the ROBUST-weighted data are given in Table 4, and compared to single-dish measurements in Figure 3. The single-dish values are taken from Bottinelli et al. (1982), Schneider et al. (1990; DDO 101), Huchtmeier et al. (2003; DDO 53, DDO 216, F564-V3), and Springob et al. (2005; CVnIdwA). Our VLA H I masses agree within 11% with those measured with single dish telescopes. However, there is some bias towards VLA interferometer masses being slightly lower than those measured with single-dish telescopes. One can see this in Figure 3 by comparing the best fit line to the data in red with the line of equal values in black.

4.2. Velocity profiles and Single-dish comparison

In general, we find good agreement between the VLA and single-dish measurements in the literature. We used spectra from the NASA Extragalactic Database, when available, and the telescopes that the single-dish measurements come from are given in Table 5. When comparing velocity profiles, we use our VLA ROBUST maps as they generally recover more flux than the Natural-weighted maps, which were cleaned to 2.5×rms rather than 2×rms. The profiles are shown in Figure 4 and details of the comparison of individual galaxies are listed in Table 5.

Galaxies that show no significant difference between the interferometer and single-aperture measurements include CVnI dwA, DDO 43, DDO 46, DDO 47, DDO 52, DDO 70, DDO 75, DDO 133, DDO 155, DDO 210, DDO 216, SagDIG, and VII Zw 403. Those that are very close in shape, but have 10% to 25% less emission in the VLA profiles include DDO 53, DDO 63, DDO 87, DDO 167, and DDO 187. Most of these differences fall within the range of measurement uncertainty, and the choices of baseline fits can also account for some of the discrepancies. Some galaxies (LGS3, M81dwA, NGC 3738, UGC 8508, Haro 36, Mrk 178) have rather noisy profiles, but generally agree in shape.

Galactic H I emission affects several of the single-dish profiles. For DDO 53, DDO 69, Sag DIG, and VII Zw 403, the addition is obvious and far enough away in velocity from the peak of the extragalactic emission that it introduces no confusion in the comparison. NGC 1569, however, is heavily affected by Galactic H I, so that the single-dish and interferometric profiles are hard to compare.

IC 10 and IC 1613 exhibit much more emission in the single-dish observations, with the VLA only recovering 40% to 50% of the peak single-dish flux. The VLA could be missing

a significant amount of emission simply because the galaxies have large angular extents. Interferometers are inherently less sensitive to emission filling a substantial fraction of the primary beam. DDO 50, DDO 69, DDO 126, DDO 165, NGC 4163, and NGC 4214 are other galaxies that show more modest examples of this behavior. The high-velocity gas in Haro 29 matches quite well with single-dish observations, but at the low-velocity side of the profile, the single-dish observations have a broad wing of low brightness material that does not show up in the VLA profile.

For galaxies that occupy a larger area on the sky than the half-power beam width of a single-dish instrument, we expect the VLA, with its relatively large HPBW, to recover more extended flux. This can show up in the form of enhanced "shoulders" or asymmetric excesses in the VLA data. Galaxies in this situation are DDO 101, DDO 154, DDO 168, F564-V3, NGC 2366, and WLM. Two single-dish profiles are presented for DDO 154 because there is some disagreement between the published single-dish data.

4.3. Surface mass densities

To construct the H I mass surface density profiles, we measured the flux in annuli on the velocity-integrated H I maps (ELLINT). We did this using the optically-defined parameters of center position, position angle of the major axis, and inclination of the galaxy. These parameters were determined from the optical V-band morphology (Hunter & Elmegreen 2006), and are given in Table 6. H I kinematic parameters are in the process of being measured as the velocity fields are determined (Oh et al., in preparation), and eventually surface density profiles will be made with the kinematic parameters. The optical inclination assumes an intrinsic minor-to-major axis ratio b/a of 0.3 (Hodge & Hitchcock 1966, van den Bergh 1988). The width of the annuli and step size for the radius of each annulus for each galaxy was chosen to be approximately that of the FWHM of the beam, and the profiles were integrated from the center of the galaxy outward until we ran out of image. The surface density profiles for the ROBUST-weighted integrated H I maps are shown in Figure 5.

5. Public data products

The H I and ancillary data are being made available to the public through NRAO. The H I data include the Naturally-weighted and ROBUST-weighted cubes and moment maps (velocity-integrated H I maps H I, intensity-weighted velocity field, intensity-weighted velocity dispersion). The ancillary data include FUV, NUV, $UBVJHK$, and Hα images, as

available for each galaxy. In addition to the images and cubes, we will include basic analysis products in tabular and graphical form as they become available. These currently include the velocity-integrated flux profiles and H I mass surface density profiles.

The NRAO web site is http://science.nrao.edu/science/surveys/littlethings, and the data can be obtained there now. The ancillary data are also available at the Lowell Observatory web site http://www.lowell.edu/users/dah/littlethings/index.html. We believe these data will be useful to the community for a wide variety of investigations.

Facilities: VLA Hall Perkins GALEX Spitzer

A.   Calibration and Combination of Data

The calibration steps followed broadly standard procedures; here we highlight those steps that needed particular attention and our "recipes" are available online. In what follows, CH0 refers to an average of the inner 75% of the frequency channels observed; LINE refers to the spectral line data set.

Data were loaded into AIPS using FILLM with the option to store channel/IF dependent weights with the visibilities, creating a CH0 and LINE file. The CH0 data were inspected for interference and other obvious problems using TVFLG. The visibilities were updated with baseline corrections from VLANT. The EVLA-EVLA baselines were flagged in their entirety.

We removed 8% of the channels, 4% on either side of the band, from the LINE data using UVCOP because the noise in the first channel would percolate through to the bandpass calibration. We subsequently proceeded with the bandpass calibration. Contrary to what was customary when reducing VLA data, we did the bandpass correction as one of the first steps, rather than as one of the last. This was to remove VLA-EVLA closure errors due to non-matched bandpass shapes between VLA and EVLA antennas.

We recreated a new CH0 using AVSPC on the LINE data and applying the bandpass correction. It is this CH0 that we then further calibrate in a fairly standard manner. We ran a number of diagnostic tests to check the quality of the calibration and to detect possible problems, notably those related to the VLA-EVLA transition period Quality control checks included using POSSM to examine the band-pass calibration done prior to constructing a new Channel 0 (CH0) (to examine the band-pass calibration table, to apply the calibration to the secondary calibrator and examine individual baselines, and to apply to the secondary calibrator as a vector average of all data), SNPLT to inspect the amplitude and phase calibration (SN) table, LISTR to look at the SN table itself and check for phase or amplitude jumps, ANBPL to check the antenna-based data weights, TVFLG to examine the uv-data as a function of baseline and time, UVPLT and WIPER to plot the amplitude and phase against uv-distance for the calibrators and galaxy with the CH0 and with the line data, IMAGR to map the calibrators and check their fluxes and map the source with the CH0 and line data, POSSM to check the vector average of all of the data for each calibrator, and computing the actual and expected S/N.

With few exceptions (see Table 3) the LITTLE THINGS galaxies were observed in three different array configurations, B, C, and D, that needed to be combined into one data set. Furthermore, multiple observing runs contributed to the data taken in each of the configurations. Some of the data came from the NRAO archive, whereas the rest were newly observed. The archival data were Hanning-smoothed whereas the new data were not.

Once calibrated, we ran task CVEL to correct the frequencies from scan to scan as well as to align all observations of each galaxy in velocity. If newly observed data were to be combined with archival observations, Hanning-smoothing was applied to the data as well, again as part of task CVEL. Although this task applies Hanning-smoothing, it does not remove every other channel, which is what used to be the case with the VLA correlator when specifying the Hanning-smoothing option. To accomplish this we used task UVDEC. Once the data sets had the same frequency resolution and sampling, they were aligned in velocity and, where required, precessed to the same J2000 epoch using UVFIX. We used task DBCON to merge them into the final dataset.

We used UVLSF, and a linear baseline, to extract the continuum based on the location

of channels free from line emission as identified in a dirty image cube of all the combined data.

B. Imaging

Interferometers measure the Fourier transform of the sky intensity distribution. However, interferometric data are affected by incomplete coverage of the aperture plane: missing zero-spacing flux and information on short-baselines, missing or deleted baselines, missing or deleted hour angle ranges. To remove the effects this incomplete coverage has on the resulting images, deconvolution algorithms were developed, notably the method known as CLEAN (Högbom 1974). Although powerful, CLEAN has its limitations, some of which we mention briefly here before we describe the approach we took.

Standard CLEAN decomposes an image into clean components (basically Dirac delta functions at grid point locations) and a residual map. The clean components convolved with the original (also known as dirty) beam, a process known as restoring, and put back on to the residual map would give the original (dirty) image back. If instead the restoration is done with a Gaussian beam that matches the resolution of the dirty beam, a cleaned map results. Usually the flux in the cleaned map is determined under the assumption that the clean beam applies, which is only true if all flux registered by the interferometer was cleaned. Because noise in the map makes it often difficult to clean down to the noise level, the residual map can contain appreciable residual signal, especially when cleaning extended structures (Jörsäter & van Moorsel 1995). The flux is calculated correctly only for the clean components retrieved from the map, for the residual map it is overestimated by a factor equal to the ratio between the dirty and clean beam (for more details, see Walter et al. 2008). For this reason, a standard clean using AIPS task IMAGR can overestimate the flux by as much as 50% as shown in Fig. 6 (bottom left panel, red line). Rescaling the flux in the residual map can be used to correct for this (Fig. 6, bottom left panel, green line), but does not deal with the fact that a substantial amount of flux has not been retrieved, and hence cleaned. This manifests itself by the emission sitting within a depression in the map (commonly referred to as the negative bowl), and in Fig. 6 (bottom left panel), by the subsequent drop after reaching a maximum when integrating a map out to ever larger radii.

Extended, low–level emission is a major contributor to the integrated flux of extended sources, even if the brightness in each pixel is at low signal–to–noise, which means that CLEAN would have to go to very low levels to recover all signal. That is difficult as CLEAN tends to diverge when reaching levels below typically $2\times$rms. To address this, Wakker & Schwarz (1988) developed an algorithm that solves sequentially, in the image plane, for

structures at increasing scale. Their algorithm formalized the concept introduced by Brinks & Shane (1984) under the name of Multi–resolution CLEAN, who ran CLEAN on an image at full resolution down to a set limit, after which the residual image and dirty beam were convolved to lower resolution and cleaned further, and so on, cleaning at 3 or 4 resolutions in total.

An extension of the Wakker & Schwarz (1988) algorithm was further developed by Cornwell as Multi–Scale CLEAN (Cornwell et al. 1999; Cornwell 2008) and implemented in AIPS by Greisen as a Multi–resolution CLEAN within AIPS task IMAGR (Greisen et al. 2009). An early implementation within the Common Astronomy Software Applications (CASA) package was tested on galaxies that are part of THINGS (Rich et al. 2008). We will refer to both of these implementations as Multi–Scale CLEAN (or MS-CLEAN for short).

MS-CLEAN deals with extended structure by using *a priori* knowledge of spatial scales expected to be present in the image. When smoothing, the ratio of the extended source structure to beam size improves, which means that what was extended in the original resolution becomes small scale in a smoothed map. Moreover, the signal to noise in a smoothed map improves as long as the structure in the map remains resolved, allowing a much deeper clean and therefore ensuring that most flux is recovered. For information on all scales to be retrieved in the AIPS implementation of MS-CLEAN, the user not only can choose the widths of circular Gaussians that will be used to make beam and data images at each scale, but also the relative importance given to small versus large scales.

The AIPS implementation of MS-CLEAN uses the multi–facets approach available in IMAGR for wide–field imaging. Whereas for wide–field imaging IMAGR creates a map made of adjacent facets, in MS-CLEAN mode IMAGR creates a map out of overlapping facets over the same area of the sky, each facet representing a different resolution scale instead. At each major cleaning cycle, it selects one of the angular scales, re–images that facet with the current residual $uv-$data, finds clean components for that facet using minor cycles and continues until it reaches one of the stopping criteria, prompting clean to go through the next major cycle. The selection of which resolution should be cleaned is done by establishing which resolution has the highest peak flux. The algorithm stops when the flux level in all facets (at each of the resolution scales) is below the user–defined flux cut–offs or the number of components cleaned has reached a set limit. Then, the clean components for all resolutions, each with their corresponding clean beam, are restored to the image made at the highest resolution (Greisen et al. 2009).

It should be stressed that the parameter choice should be carefully tuned to the data set to be imaged. The algorithm available under the IMAGR task in AIPS requires a number of input parameters. The first two of them are NGAUS and WGAUS representing the number

of scales to clean simultaneously and the approximate width of the convolution kernel used, in arcseconds. We applied the algorithm to images with data collected in B, C, and D-configurations, i.e., with a substantial range of angular scales (spatial frequencies). After several tests (see Fig. 6, top left panel) we decided to use four kernels with widths of $0''$ (i.e., native resolution), $15''$, $45''$, and $135''$.

FGAUS allows the user to impose a stopping criterion for each resolution. We established our rms noise threshold by measuring the noise at each of the four resolutions of a dirty, line–free channel. Consequently, we have four different noise levels, one for each field. The four cut–off levels to be set in FGAUS are not independent, being different smoothed versions of the same dataset. We investigated different flux cut–offs, trying both deeper cleaning, down to $1\times$rms and $1.5\times$rms and more superficial cleaning to $3\times$rms and $5\times$rms. We plot the integrated flux as a function of radius in Fig. 6 (top right panel). We find that cleaning down to 3 or $5\times$rms is not sufficient as we are not retrieving all the flux and evidence for a "negative bowl" is seen at large radii. Cleaning down to 1 or $1.5\times$rms does not retrieve more flux than cleaning down to $2\times$rms; however, clean artifacts start to become noticeable in the final image. This implies we do not need to go any deeper than $2\times$rms to retrieve all the observed flux. We therefore decided for LITTLE THINGS on cut–off levels of $2\times$rms for ROBUST-weighted data cubes and 2.5σ for the Natural-weighted cubes.

Naively one would always look for the peak residual at any resolution, and choose the next clean component based on the highest value found. However, since the lower resolutions dominate in terms of flux, the algorithm would be biased towards the largest scales (Greisen et al. 2009). To balance this, peak fluxes can be weighted by a factor of $1/[(\text{field beam area})/(\text{minimum beam area})]^{\alpha}$. Here α provides control over which resolution is going to be chosen next. If $\alpha = 0$, the peak fluxes at each resolution are unaltered; if $\alpha = 1$, the peak flux at the highest resolution will be the true peak flux, while the peak flux at all other resolutions will be down weighted. In the AIPS implementation of MS-CLEAN, α is set by the parameter IMAGRPRM(11).

To illustrate how this biasing works we plot the choice of resolution in each major cycle when cleaning one channel (Fig. 7). We ran tests on the choice of α and we found that for all α, the cleaning process converges. Also, the total retrieved flux is very similar. We found that a value of $\alpha = 0.2$ strikes the right compromise, with the clean alternating among the different spatial scales and thus finding emission across a range of angular scales rather than being fixated on one particular value. The effect of different values for α on the integrated flux is shown in Fig. 6 for both ROBUST and Natural-weighted data.

The differences between $\alpha = 0.2$ or 0.4 become more noticeable when looking at the final and residual maps resulting from applying MS-CLEAN to a line channel for two different

sources, DDO 168 and DDO 133 (see Figs. 8 and 9). It is clear that a particular choice for α depends on the complexity of the source to be imaged. Although there is little difference in the final maps for DDO 168, in the case of DDO 133 there are signs of over–cleaning for $\alpha = 0.4$.

As an aside, it is interesting to note to what extent the residual scaled standard CLEAN follows the Natural-weighted MS-CLEAN results, even at larger radii, which was not the case for the ROBUST=0 MS-CLEAN case (see Fig. 6, bottom right panel). This is not an effect of MS-CLEAN, but rather a consequence of the different density of visibilities near the center of the $uv-$plane and the different manners this is dealt with in the weighting scheme employed, Natural versus ROBUST.

Other than those described above, all further parameters were left at their default values. If we compare MS-CLEAN and traditional CLEANing methods we find that in our test the standard CLEAN has a peak flux which is 40% higher than the MS-CLEAN or residual scaled CLEAN (see Fig. 6, bottom left panel). This shows that MS-CLEAN, unlike standard CLEAN, properly addresses the problem related to determining the total flux. At the same time MS-CLEAN recovers all measured flux much better than the standard CLEAN, reducing considerably the negative bowl problem in extended sources. As a caveat, MS-CLEAN does not recover flux that was not measured at spacings shorter than the shortest spacing partaking in the observation. Therefore, any emission on scales more extended than those present in the observation will be missing.

As a final check, we looked into the noise characteristics of MS-CLEAN. In Fig. 10 we present noise histograms for different choices of α corresponding to the cleaned maps at full resolution, and the 15″ and 45″ residual maps and compare these with noise histograms on a line free channel at the same scales. We see that MS-CLEAN does not affect the nature of the noise in any of the maps shown (the tail to positive intensities in rows 2, 3, and 4, reflects genuine emission).

C.   The Data

We present the basic data for each galaxy in Figures 11 to 90. Figures 11 and 12 are shown here, and the rest are available on-line. Each galaxy has two pages: the channel maps and a combination of images. The requirement for the channel maps was that each galaxy fit on one page, and so some have binned pixels and none show every channel. However, we show the full range of channels with emission. On the image page, the false color image in the upper left combines the integrated H I map (red), V (green), and FUV (blue) and allows one

to see the relationship of the gas and stars. The other images are the first three moment maps from the Naturally-weighted cube: velocity-integrated H I, flux-weighted velocity field, and flux-weighted velocity dispersion for each galaxy. All of the flux-weighted velocity dispersion maps (moment two) were made with a scale of 0 (dark blue) to 15 km s^{-1} (red).

REFERENCES

Asplund, M., Grevesse, N., Sauval, A. J., & Scott, P. 2009, ARA&A, 47, 481

Baars, J. W. M., Genzel, R., Pauliny-Toth, I. I. K., & Witzel, A. 1977, A&A, 61, 99

Bastian, N., Ercolano, B., Gieles, M., et al. 2007, MNRAS, 379, 1302

Bigiel, F., Leroy, A., Walter, F., Blitz, L., Brinks, E., de Blok, W. J. G., & Madore, B. 2010, AJ, 140, 1194

Bottinelli, L., Gouguenheim, L., Fouqué, P., & Paturel, G. 1990, A&AS, 82, 391

Briggs, D. 1995, PhD thesis. New Mexico Institute of Mining and Technology

Brinks, E., & Shane, W. W. 1984, A&AS, 55, 179

Burstein, D., & Heiles, C. 1984, ApJS, 54, 33

Comins, N. E. 1983, ApJ, 266, 543

Cornwell, T. J. 2008, IEEE Journal of Selected Topics in Signal Processing, 2, 793

Cornwell, T., Braun, R., & Briggs, D. S. 1999, in Astronomical Society of the Pacific Conference Series, Vol. 180, Synthesis Imaging in Radio Astronomy II, ed. G. B. Taylor, C. L. Carilli, & R. A. Perley, 151

Croxall, K. V., van Zee, L., Lee, H., et al. 2009, ApJ, 705, 723

Dalcanton, J. J., Williams, B. F., Seth, A. C., et al. 2009, ApJS, 183, 67

Dale, D. A., Cohen, S. A., Johnson, L. C., Schuster, M. D., Calzetti, D., et al. 2009, ApJ, 703, 517

de Grijs, R., Kregel, M., & Wesson, K. 2001, MNRAS, 324, 1074

de Vaucouleurs, G., de Vaucouleurs, A., & Corwin, H. 1976, Second Reference Catalogue of Bright Galaxies, (Austin:University of Texas Press)

de Vaucouleurs, G., de Vaucouleurs, A., Corwin, H., et al. 1991, Third Reference Catalogue of Bright Galaxies, New York: Springer-Verlag

Dickey, J. M., McClure-Griffiths, N. M., Stanimirović, S., Gaensler, B. M, & Green, A. J, 2001, ApJ, 561, 264

Dolphin, A. E., Saha, A., Claver, J., et al. 2002, AJ, 123, 3154

Dolphin, A. E., Saha, A., Skillman, E. D., et al. 2003, AJ, 125, 1261

Dopita, M. A., Mathewson, D. S., & Ford, V. L. 1985, ApJ, 297, 599

Eder, J. A., & Schombert, J. M. 2000, ApJS, 131, 47

Efremov, Y. N., & Elmegreen, B. G. 1998, MNRAS, 299, 588

Elmegreen, B. G., Kim, S., & Staveley-Smith, L. 2001, ApJ, 548, 749

Erwin, P., Pohlen, M., & Beckman, J. E. 2008, AJ, 135, 20

Freedman, W. L., Madore, B. F., Gibson, B. K., et al. 2001, ApJ, 553, 47

Gerola, H., Seiden, P. E., & Schulman, L. S. 1980, ApJ, 242, 517

Gieren, W., Pietrzyński, G., Nalewajko, K., et al. 2006, ApJ, 647, 1056

Gieren, W., Pietrzyński, G., Szewczyk, O., et al. 2008, ApJ, 683, 611

Giovanelli, R., Haynes, M. P., Kent, B. R., et al. 2007, AJ, 133, 2569

González-Delgado, R. M., Perez, E., Tenorio-Tagle, G., et al. 1994, ApJ, 437, 239

González-Riestra, R., Rego, M., & Zamorano, J. 1988, A&A, 202, 27

Greisen, E. W., Spekkens, K., & van Moorsel, G. A. 2009, AJ, 137, 4718

Grocholski, A. J., Aloisi, A., van der Marel, R. P., et al. 2008, ApJ, 686, 79

Gutiérrez, L., Erwin, P., Aladro, R., & Beckman, J. E. 2011, AJ, 142, 145

Heesen, V., Rau, U., Rupen, M. P., Brinks, E., & Hunter, D. A. 2011, ApJ, 739, L23

Herrmann, K. A., Hunter, D. A., & Elmegreen, B. G. 2012, AJ, submitted

Hibbard, J. E., van Gorkom, J. H., Rupen, M. P., & Schiminovich, D. S., 2001, in ASP Conf. Ser. 240, Gas & Galaxy Evolution, eds. J. E. Hibbard, M. P. Rupen, & J. H. van Gorkom, (ASP, San Francisco), p 659

Högbom, J. A. 1974, A&AS, 15, 417

Huchtmeier, W. K., & Seiradakis, J. H. 1985, A&A, 143, 216

Huchtmeier, W. K., & Richter, O. G. 1986, A&AS, 63, 323

Huchtmeier, W. K., Karachentsev, I. D., & Karachentseva, V. E. 2003, A&A, 401, 483

Hodge, P. W., & Hitchcock, J. L. 1966, PASP, 78, 79

Holmberg, E. 1958, Medd. Lunds Astr. Obs., 2, No. 136, 91

Hunter, D. A. 2008, in Low Metallicity Star Formation: From the First Stars to Dwarf
      Galaxies, Proceedings of IAU Symposium No. 255, eds. L.K. Hunt, S. Madden & R.
      Schneider (Cambridge: Cambridge Univ Press), p 226

Hunter, D. A., & Elmegreen, B. G. 2004, AJ, 128, 2170

Hunter, D. A., & Elmegreen, B. G. 2006, ApJS, 162, 49

Hunter, D. A., Elmegreen, B. G., & Baker, A. 1998, ApJ, 493, 595

Hunter, D. A., Elmegreen, B. G., & Ludka, B. C. 2010, AJ, 139, 447

Hunter, D. A., Elmegreen, B. G., & Martin, E. 2006, AJ, 132, 801

Hunter, D. A., & Gallagher, J. S. III 1985, AJ, 90, 1789

Hunter, D. A., & Hoffman, L. 1999, AJ, 117, 2789

Jörsäter, S., & van Moorsel, G. A. 1995, AJ, 110, 2037

Johnson, M., Hunter, D. A., Oh, S.-H., et al. 2012, AJ, submitted.

Karachentsev, I. D., Dolphin, A. E., Geisler, D., et al. 2002, A&A, 383, 125

Karachentsev, I. D., Dolphin, A., Tully, R. B., et al. 2006, AJ, 131, 1361

Karachentsev, I. D., Karachentseva, V., E., Huchtmeier, W. K., & Makarov, D. I. 2004, AJ,
      127, 2031

Karachentsev, I. D., Makarov, D. I., Sharina, M. E., et al. 2003a, A&A, 398, 479

Karachentsev, I. D., Sharina, M. E., Dolphin, A. E., et al. 2003b, A&A, 398, 467

Kniazev, A. Y., Grebel, E. K., Pustilnik, S. A., Pramskij, A. G., & Zucker, D. B. 2005, AJ, 130, 1558

Kobulnicky, H. A., & Skillman, E. D. 1997, ApJ, 489, 636

Koribalski, B. S., Staveley-Smith, L., Kilborn, V. A., et al. 2004, AJ, 128, 16

Kregel, M., & van der Kruit, P. C. 2004, MNRAS, 355, 143

Kregel, M., van der Kruit, P., & de Grijs, R. 2002, MNRAS, 334, 646

Lee, H., Grebel, E. K., & Hodge, P. W. 2003a, A&A, 401, 141

Lee, H., McCall, M. L., Kingsburgh, R. L., Ross, R., & Stevenson, C. C. 2003b, AJ, 125, 146

Lee, H., Skillman, E. D., & Venn, K. A. 2005, ApJ, 620, 223

Lequeux, J., Peimbert, M., Rayo, J. F., Serrano, A., & Torres-Peimbert, S. 1979, A&A, 80, 155

Lewis, B. M., Helou, G., & Salpeter, E. E. 1985, ApJS, 59, 161

Lynds, R., Tolstoy, E., O'Neil, E. J., Jr., & Hunter, D. A. 1998, AJ, 116, 146

Martin, D. C., Fansom, J., Schiminovich, D., et al. 2005, ApJ, 619, L1

Masegosa, J., Moles, M., & del Olmo, A. 1991, A&A, 249, 505

Mac Low, M.-M., & Klessen, R. 2004, Rev Mod Phys, 76, 125

Méndez, B., Davis, M., Moustakas, J., Newman, J., Madore, B. F., & Freedman, W. L. 2002, AJ, 124, 213

Meschin, I., Gallart, C., Aparicio, A., Cassisi, S., & Rosenberg, A. 2009, ApJ, 137, 3619

Miller, B. W., Dolphin, A. E., Lee, M. O., Kim, S. C., & Hodge, P. 2001, ApJ, 562, 713

Momany, Y., Held, E. V., Saviane, I., & Rizzi, L. 2002, A&A, 384, 393

Mori, M., Yoshii, Yl, Tsujimoto, T., & Nomoto, K. 1997, ApJ, 478, 21

Mould, J. R., Huchra, J. P., Freedman, W. L., et al. 2000, ApJ, 529, 786

Moustakas, J., & Kennicutt, R. C., Jr. 2006, ApJS, 164, 81

Moustakas, J., Kennicutt, R. C., Jr., Tremonti, C. A., et al. 2010, ApJS, 190, 233

Öpik, E. J. 1953, ItAJ, 2, 219

Ott, J., Warren, S., Stilp, A., et al. 2010, Bulletin of the American Astronomical Society, 42, 293

Pérez, I. 2004, A&A, 427, L17

Pietrzynski, G., Gieren, W. l., Soszynski, I., et al. 2006, ApJ, 642, 216

Pilbratt, G. L., Riedinger, J. R., Passvogel, T., et al. 2010, A&A, 518, 1

Pohlen, M., Dettmar, R.J., Lütticke, R., & Aronica, G. 2002, A&A, 392, 807

Pohlen, M., & Trujillo, I. 2006, A&A, 454, 759

Rich, J. W., de Blok, W. J. G., Cornwell, T. J., et al. 2008, AJ, 136, 2897

Richer, M. G., & McCall, M. L. 1995, ApJ, 445, 642

Rots, A. H. 1980, A&AS, 41, 189

Sakai, S., Ferrarese, L., Kennicutt, R. C., Jr., & Saha, A. 2004, ApJ, 608, 42

Sakai, S., Madore, B. F., & Freedman, W. L. 1999, ApJ, 511, 671

Schulte-Ladbeck, R. E., Hopp, U., Greggio, L., Crone, M. M., & Drozdovsky, I. O. 2001, AJ, 121, 3007

Schneider, S. E., Thuan, T. X., Magri, C., & Wadiak, J. E. 1990, ApJS, 72, 245

Schneider, S. E. 1992, ApJS, 81, 5

Shostak, G. S., & Allen, R. J. 1980, A&A, 81, 167

Skillman, E. D., Bomans, D. J., & Kobulnicky, H. A. 1997, ApJ, 474, 205

Skillman, E. D., Kennicutt, R. C., & Hodge, P. W. 1989, ApJ, 347, 875

Springob, C. M., Haynes, M. P., Giovanelli, R., & Kent, B. R. 2005, ApJS, 160, 149

Stanimirović, S., Staveley-Smith, L., Dickey, J. M., Sault, R. J., & Snowden, S. L. 1999, MNRAS, 302, 417

Thuan, T. X., & Martin, G. E. 1981, ApJ, 247, 823

Tolstoy, E., Saha, A., Hoessel, J. G., & Danielson, G. E. 1995a, AJ, 109, 579

Tolstoy, E., Saha, A., Hoessel, J. G., & McQuade, K. 1995b, AJ, 110, 1640

van den Bergh, S. 1988, PASP, 100, 344

van Dyk, S. D., Puche, D., & Wong, T. 1998, AJ, 116, 2341

van Zee, L., & Haynes, M. P. 2006, ApJ, 636, 214

van Zee, L., Skillman, E. D., & Haynes, M. P. 2006, ApJ, 637, 269

Viallefond, F., & Thuan, T. X. 1983, ApJ, 269, 444

Vogelaar, M. G. R., & Terlouw, J. P. 2001, in Astronomical Data Analysis Software Systems I, eds D. M. Worall, C. Biemesderfer, and J. Barnes, ASP Conference Serices No. 25, p 131

Wakker, B. P., & Schwarz, U. J. 1988, A&A, 200, 312

Walter, F., Brinks, E., de Blok, W. J. G., et al. 2008, AJ, 136, 2563

Wilcots, E. M., & Miller, B. W. 1998, AJ, 116, 2363

Willett, K. W., Elmegreen, B. G., & Hunter, D. A. 2005, AJ, 129, 2186

Young, L. M., & Lo, K. Y. 1997, ApJ, 490, 710

Young, L. M., van Zee, L., Lo, K. Y., Dohm-Palmer, R. C., & Beierle, M. E. 2003, ApJ, 592, 111

Zhang, H.-X., Hunter, D. A., & Elmegreen, B. G., 2012a, ApJ, 754, 29.

Zhang, H.-X., Hunter, D. A., Elmegreen, B. G., Gao, Y., & Schruba, A. 2012b, AJ, 143, 47.
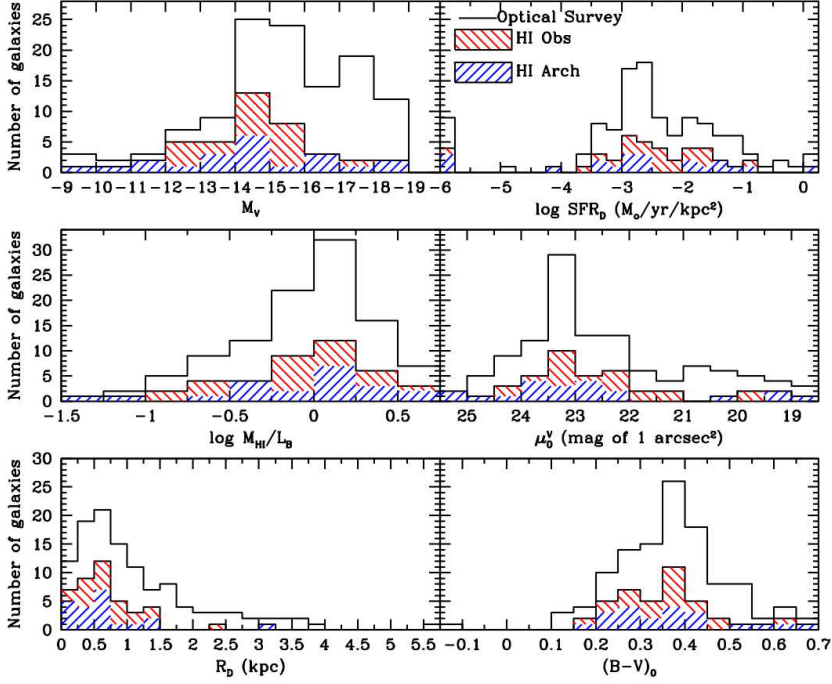
Fig. 1.— Properties of the LITTLE THINGS sample (new VLA observations [*hashed* +45°] and archive data [*hashed* −45°]) compared to the entire optical survey of Hunter & Elmegreen (2006; *no hash*). The LITTLE THINGS sample covers the range of parameters of the full survey. SFR_D is the star formation rate, based on Hα emission, normalized to πR_D^2, where R_D is the disk scale length determined from a V-band image. A star formation rate per unit area of 0 is plotted as a log of −6. The parameter μ_0^V is the central surface brightness determined from a fit to the V-band surface brightness profile. The distance dependent parameters M_V and R_D use the distances given in Table 1 for the LITTLE THINGS sample and the distances given by Hunter & Elmegreen (2006) for the rest of the galaxies in the larger optical survey sample.
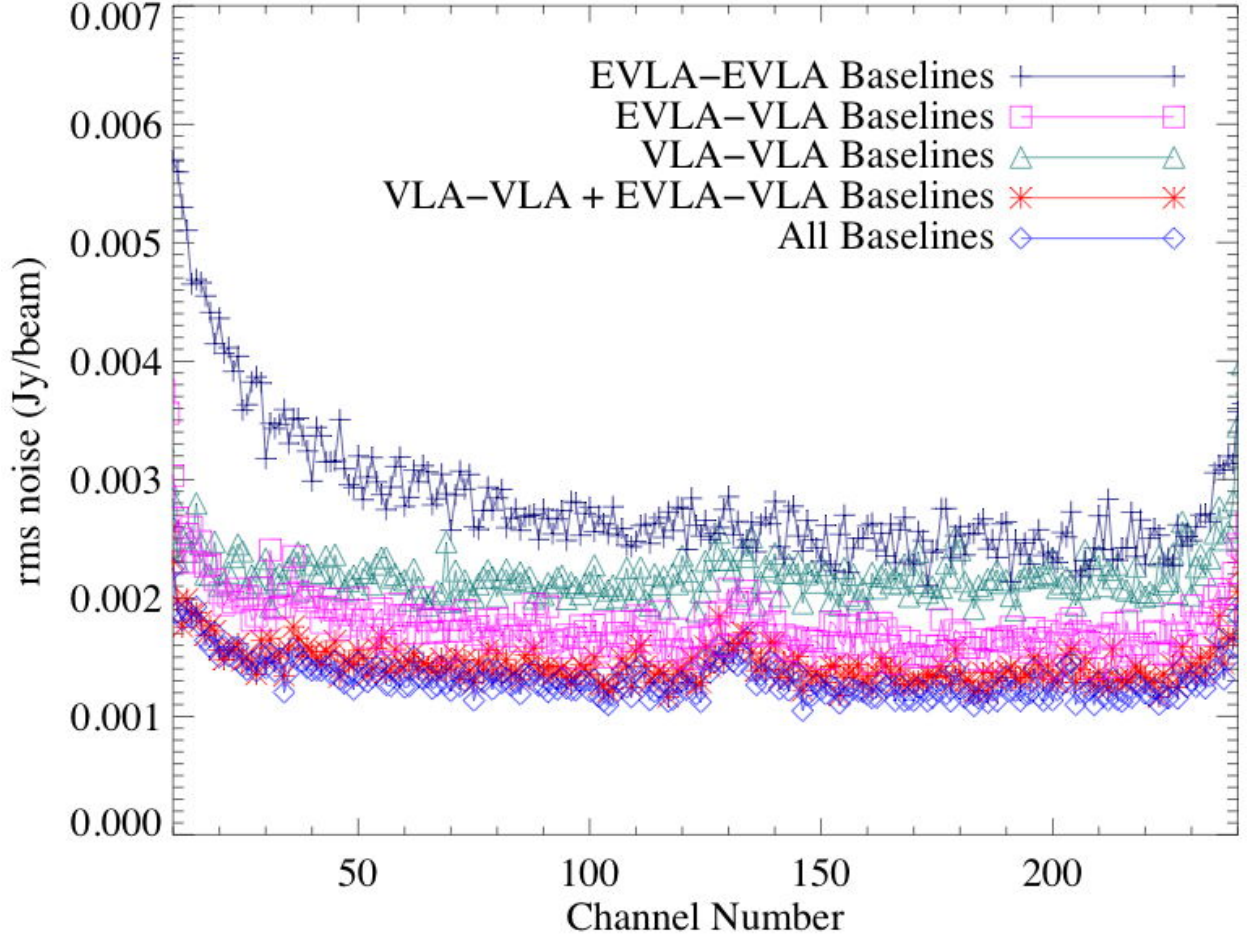
Fig. 2.— Noise level as a function of channel number for data obtained in B–configuration on DDO 43. The total bandwidth was 1.56 MHz split into 256 frequency channels. The observations were made with 26 antennas, 12 of which were equipped with the new EVLA front–ends, during the VLA–EVLA transition period. We show here different combinations of baselines: combination of 66 EVLA–EVLA baselines (navy crosses); 91 VLA–VLA baselines (green triangles); the sum of 168 VLA–EVLA baselines (open magenta squares); the combination of the VLA–VLA plus VLA–EVLA baselines (red stars); and finally all 325 baselines (open blue diamonds). Continuum emission was aliased, with phase information scrambled making it resemble noise, the effect being strongest in channels closest to the baseband edge. This is most noticeable on EVLA-EVLA baselines, and to a lesser extent on EVLA-VLA baselines; VLA-VLA baselines were not affected.
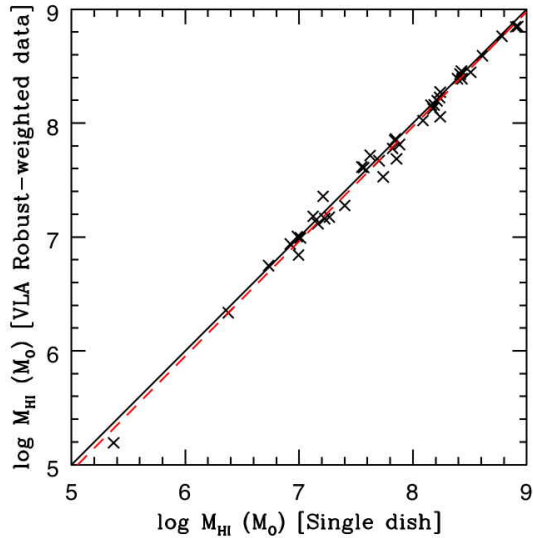
Fig. 3.— Comparison of our integrated H I masses with those from single-dish radio telescope observations. Both measurements are relative to the same distance. Our H I masses are measured on the VLA integrated H I ROBUST-weighted map. The solid black line marks equal masses, and the red dashed line is the best fit to the data. The average difference between the masses measured from the ROBUST-weighted maps and those measured from the Natural-weighted maps is 11%. The best fit line lies slightly below the line of equal masses, indicating that the VLA has systematically missed some flux compared to single-dish values.
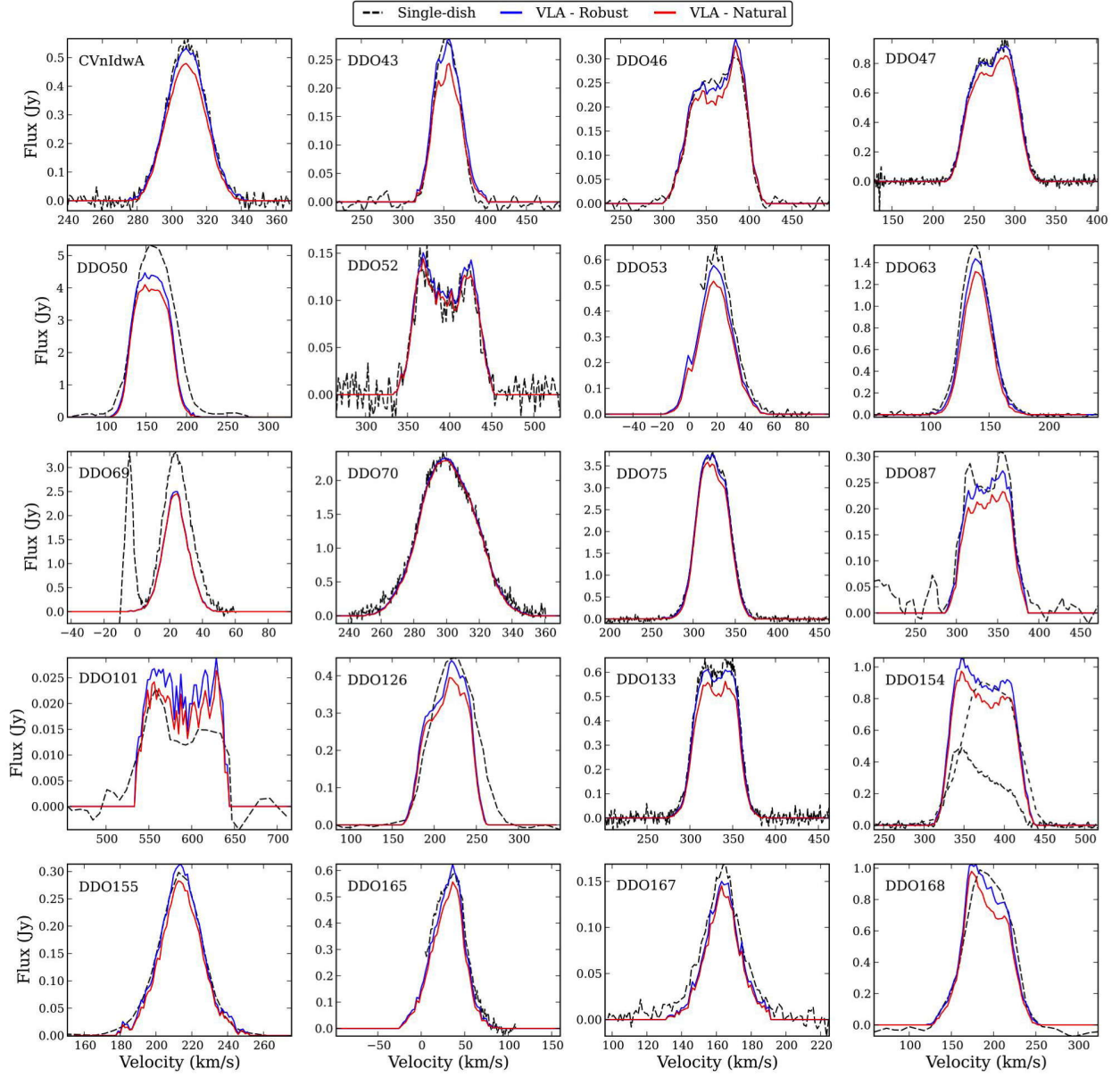
Fig. 4.— Intensity-velocity plots for each galaxy made from summing the flux in each channel of the Hanning-smoothed Naturally-weighted (*red*) and ROBUST-weighted (*blue*) H I cubes. Single-dish profiles are also shown (*black*; see Table 5 for references).
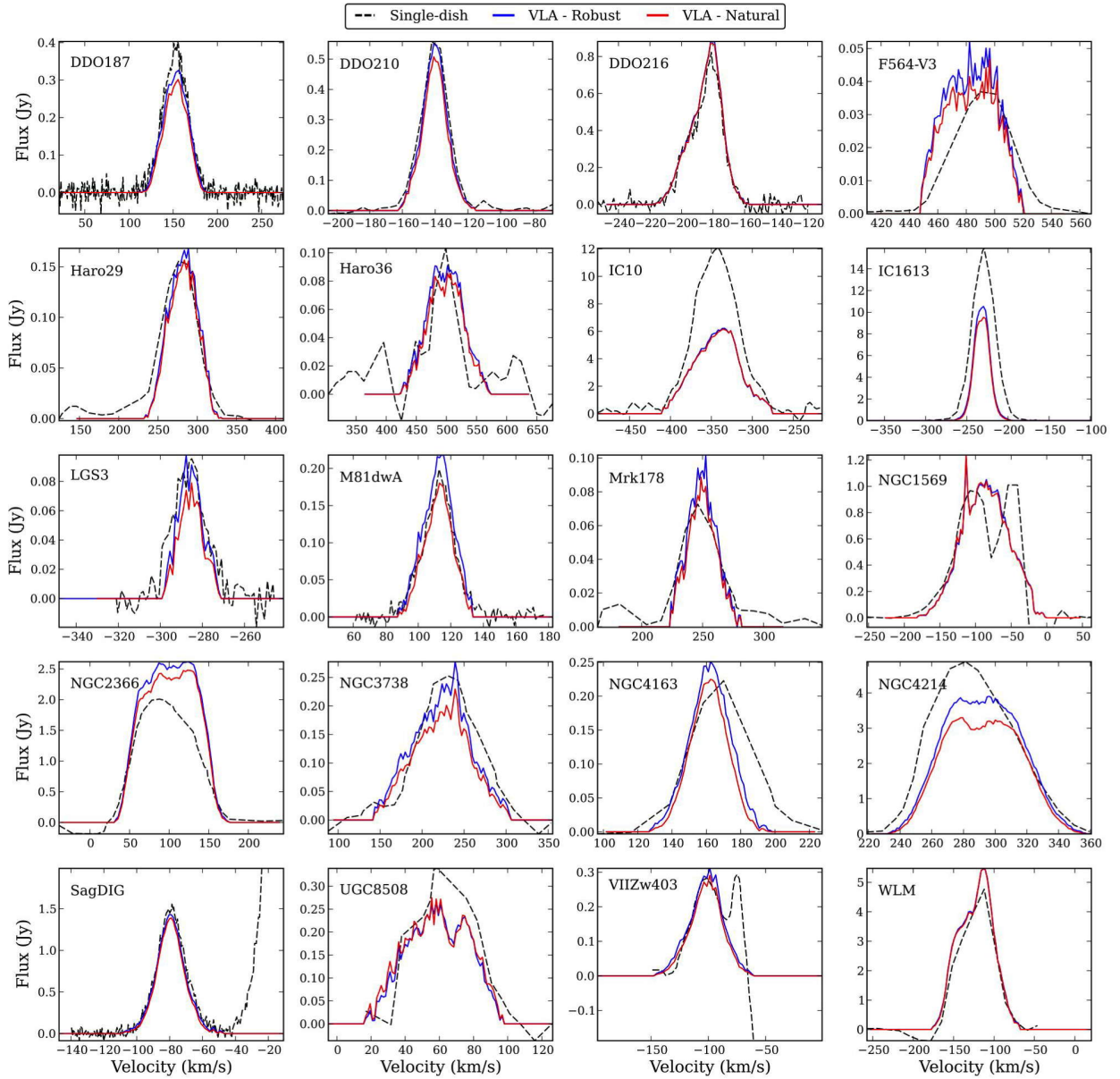
Figure 4 (continued)
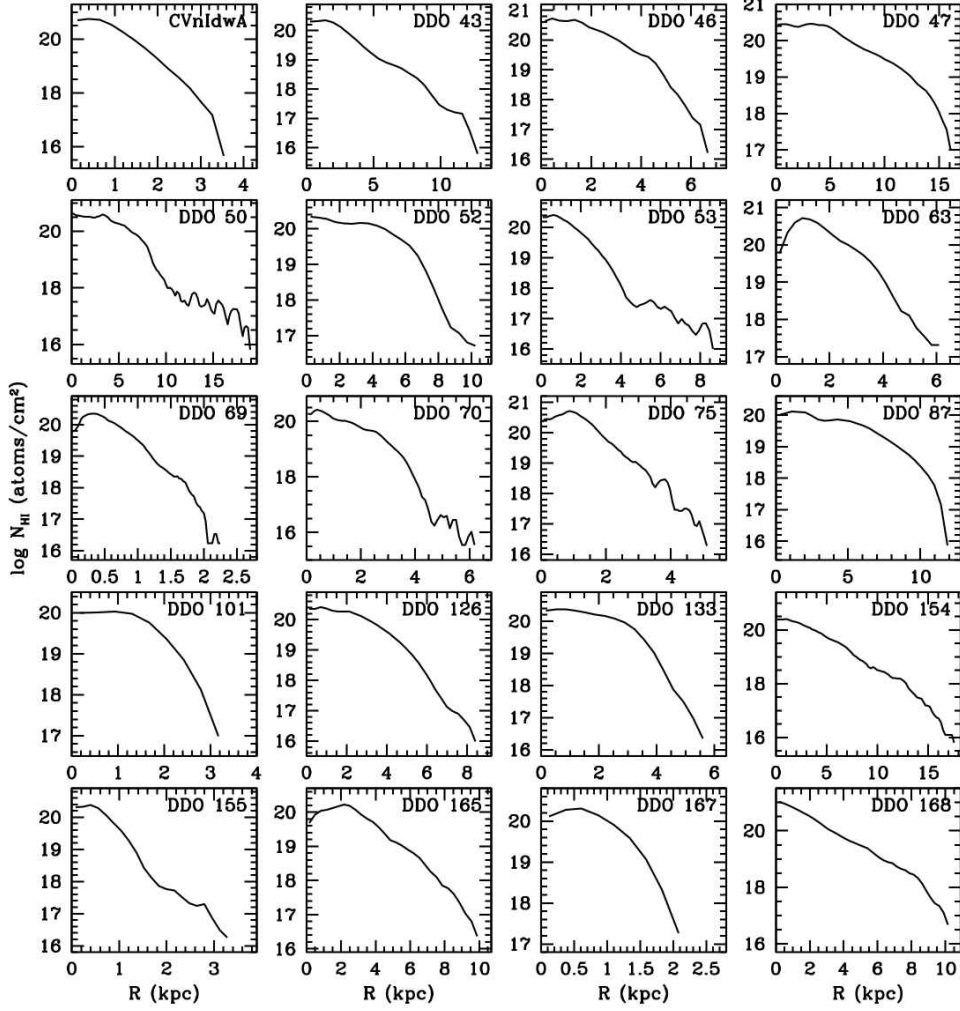
Fig. 5.— Azimuthally-averaged H I surface density as a function of distance from the center of the galaxy. These are measured from the ROBUST-weighted velocity-integrated H I maps, using parameters—center position, position angle of the major axis, and inclination of the galaxy—determined from the optical V-band morphology (see Table 6; Hunter & Elmegreen 2006). The width of the annuli and step size for the radius of each annulus was chosen to be approximately that of the FWHM of the VLA beam.
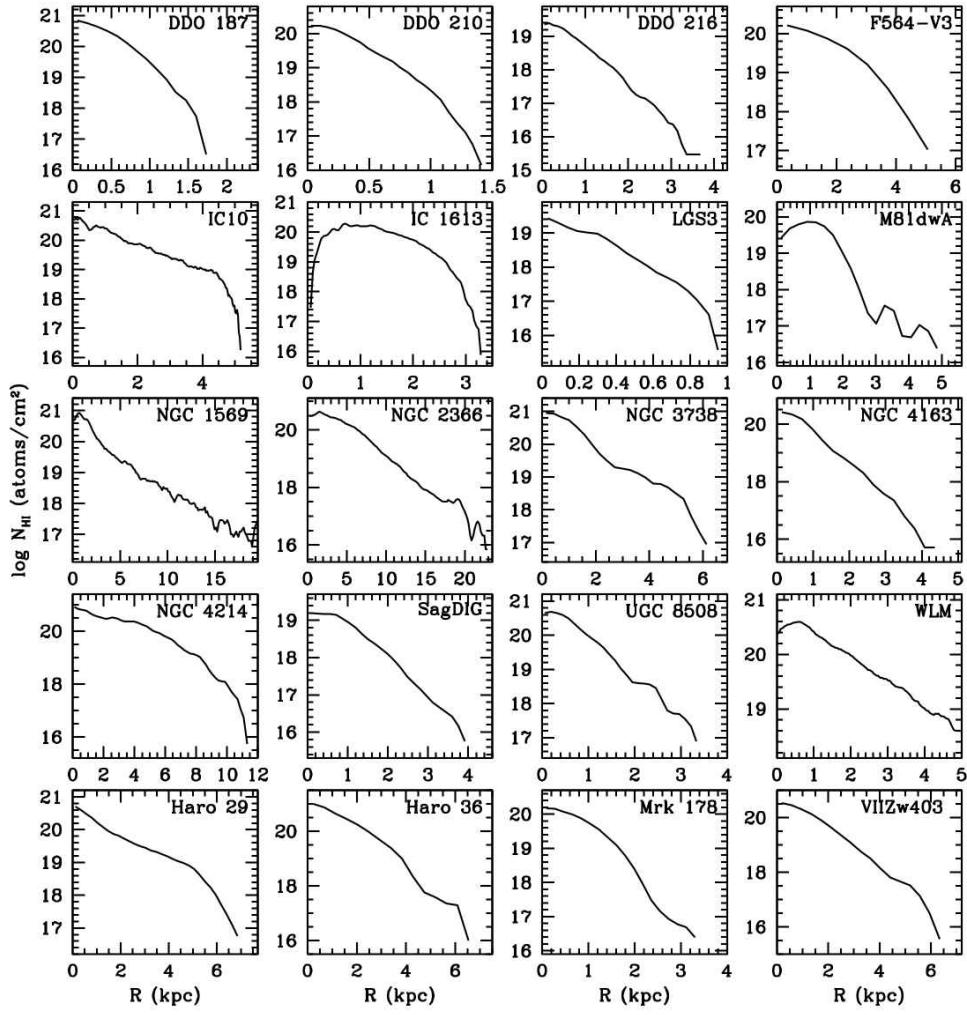
Figure 5 (continued)
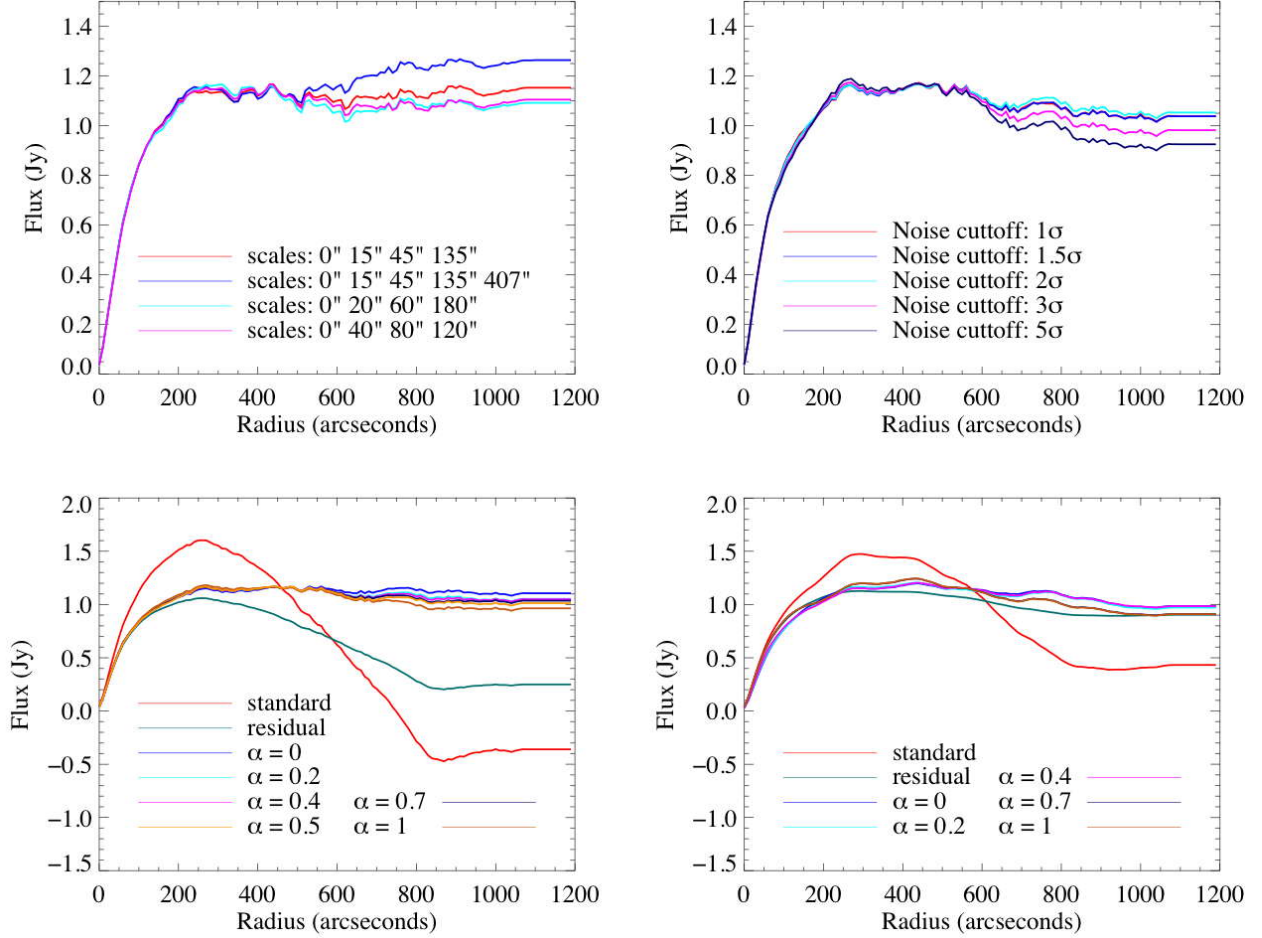
Fig. 6.— Integrated Flux density versus radius in DDO 168, channel 60, B+C+D–configurations combined. *Top Left:* Results obtained using MS-CLEAN with $\alpha = 0.2$, robust $= 0$, and testing different combinations of angular scales (red: 0, 15″, 45″, 135″; blue: 0, 15″, 45″, 135″, 407″; cyan: 0, 20″, 60″, 180″; magenta: 0, 40″, 80″, 120″). *Top Right:* Results obtained using MS-CLEAN with $\alpha = 0.2$, robust $= 0$, and testing variable flux cutoffs (red: 1σ; blue: 1.5σ; cyan: 2σ; magenta: 3σ; navy: 5σ). *Bottom Left:* Results obtained by cleaning down to 2σ, robust $= 0$, and testing dependence on α (red: standard CLEAN, green: residual scaled CLEAN, blue: MS-CLEAN and $\alpha = 0$, cyan: $\alpha = 0.2$, magenta: $\alpha = 0.4$, orange: $\alpha = 0.5$, navy: $\alpha = 0.7$, brown: $\alpha = 1$). *Bottom Right:* As Bottom Left, but with natural weight.
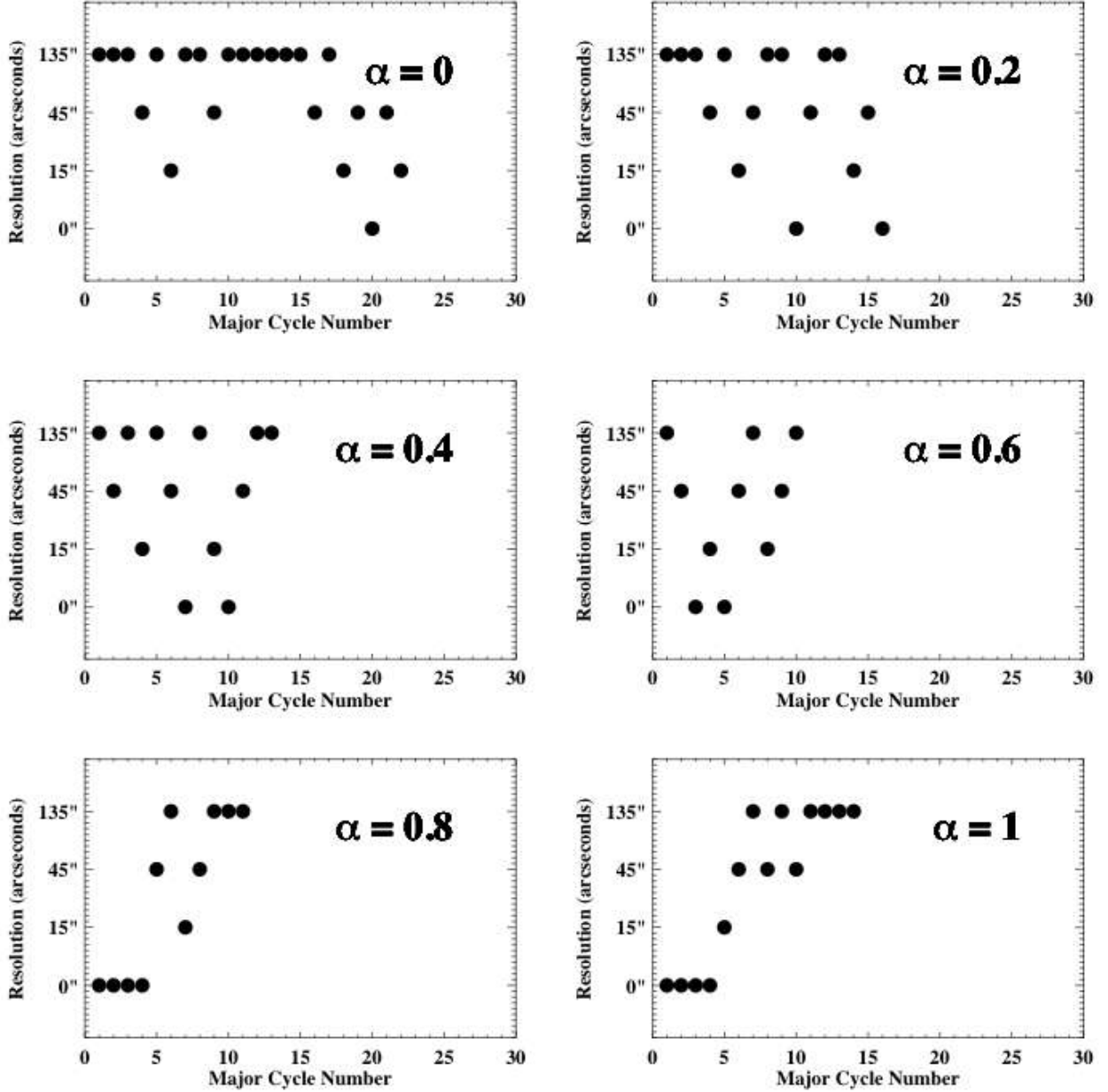
Fig. 7.— Testing the α parameter on DDO 168, channel 60, B+C+D–configurations combined. We plot the choice of resolution scale in each major cycle for $\alpha =$ $0, 0.2, 0.4, 0.6, 0.8, 1.0$. The parameter α provides control over which resolution is chosen next. If $\alpha = 0$, the peak fluxes at each resolution are unaltered; if $\alpha = 1$, the peak flux at the highest resolution will be the true peak flux, while the peak flux at all other resolutions will be down weighted. We found that a value of $\alpha = 0.2$ strikes the right compromise, with the clean alternating among the different spatial scales and thus finding emission across a range of angular scales rather than being fixated on one particular value.
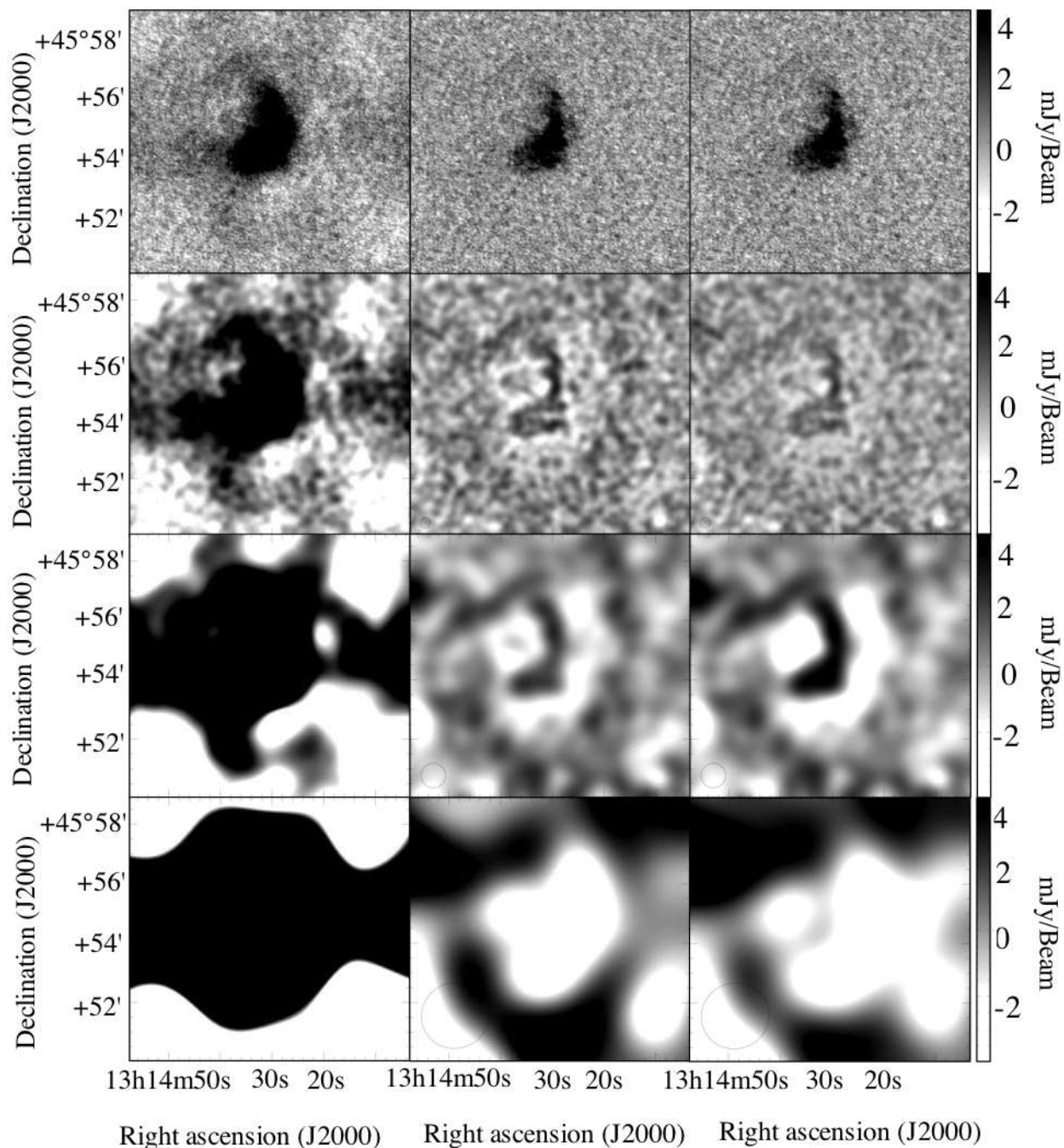
Fig. 8.— DDO 168, channel 60, B+C+D–configurations combined: Comparison between 2×rms cut–off level, robust 0.5, clean maps (*top*) and residual maps for 15″ (*second row*), 45″ (*third row*) and 135″ (*fourth row*) for $\alpha = 0.2$ (*middle column*) and $\alpha = 0.4$ (*right column*). The beam size is shown in the bottom left corner of each figure of the middle and right columns. In the first column we show as reference the uncleaned map for each field. All panels of the figure use the same grey scale, shown on the right hand side.
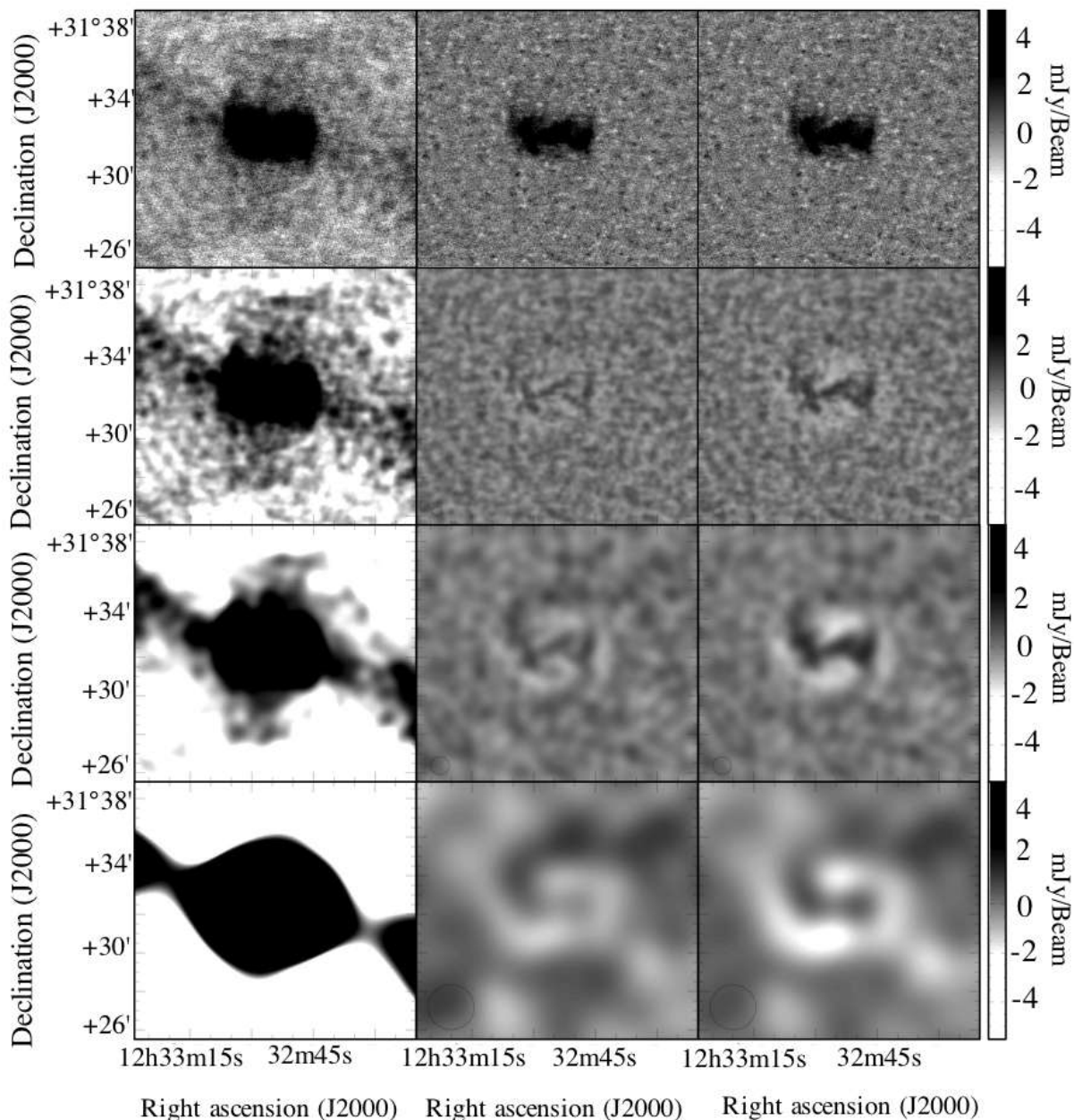
Fig. 9.— DDO 133 channel 56, B+C+D–configurations combined: Comparison between 2×rms cut–off level, robust 0.5, clean maps (*top*) and residual maps for 15″ (*second row*), 45″ (*third row*) and 135″ (*fourth row*) for $\alpha = 0.2$ (*middle column*) and $\alpha = 0.4$ (*right column*). The beam size is shown in the bottom left corner of each figure of the middle and right columns. In the left column we show as reference the uncleaned map for each field. All panels of the figure use the same grey scale, shown on the right hand side.
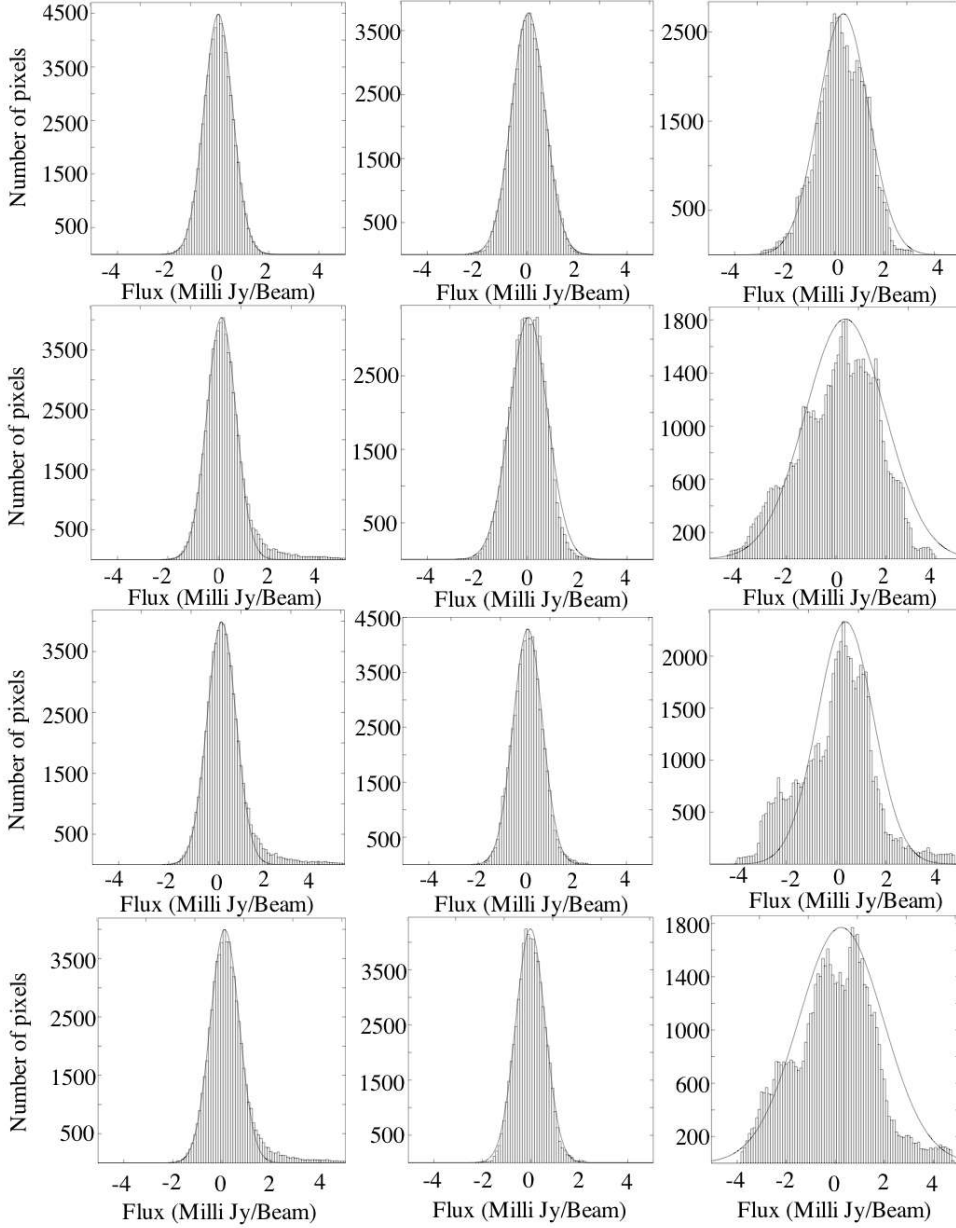
Fig. 10.— Histogram of the intensities in a single channel of DDO168, B+C+D–configurations. The row at the top is for reference and represents the distribution in a line–free channel, channel 87, robust = 0.5, and without any cleaning applied. The first column corresponds to the full resolution maps, second column to the 15″ residual map and the third column to the 45″ residual map. Rows 2, 3, and 4 are histograms of a line channel, channel 60, cleaned using MS-CLEAN with different values for α, from top to bottom: $\alpha = 0$, $\alpha = 0.2$, and $\alpha = 0.4$. Note that the first column corresponds to the final (cleaned and restored) map which explains the tail to high intensities; the remaining results are based on residual maps.
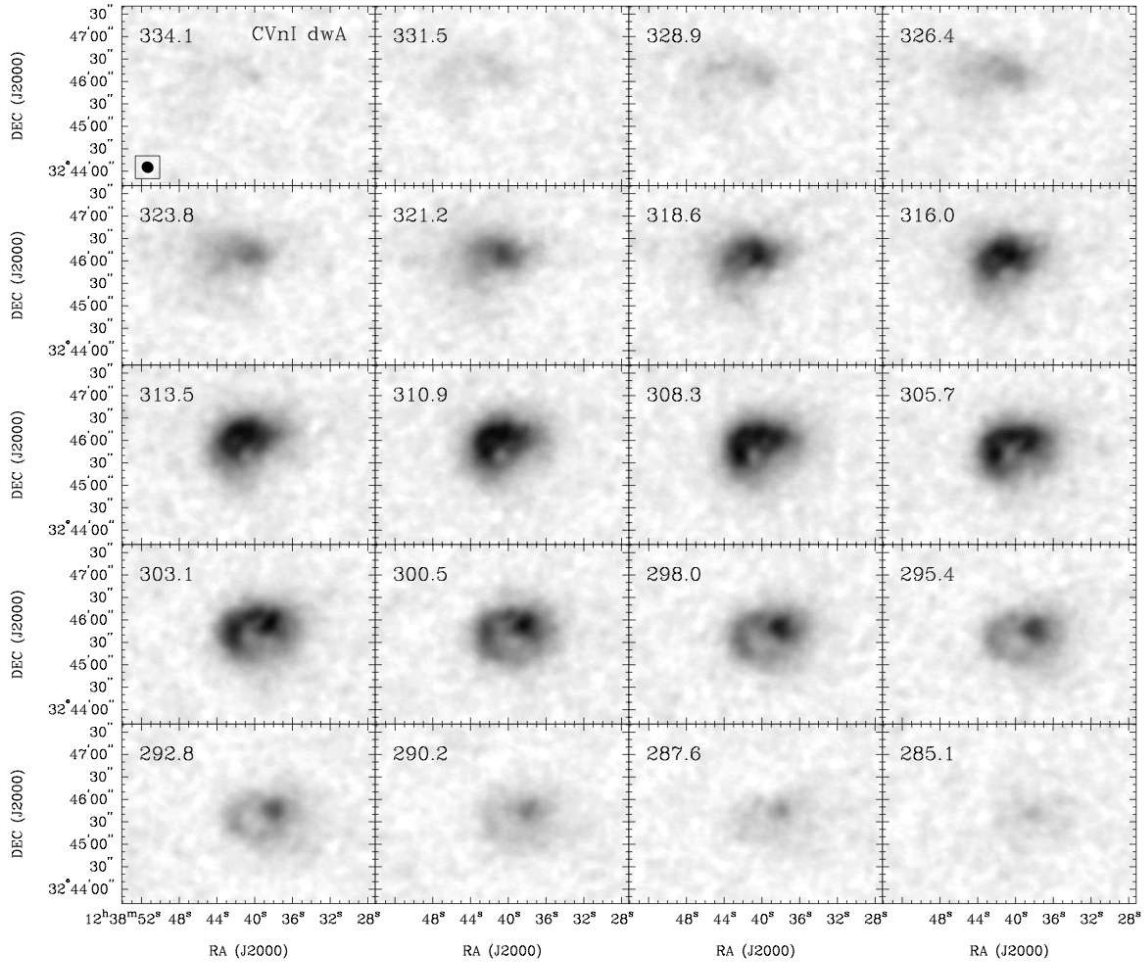
Fig. 11.— Channel maps for CVnIdwA made from the Hanning-smoothed Naturally-weighted H I-line cube. The synthesized beam is given in the left bottom corner of the top left panel. In each panel we give the observed radial velocity in km s^{-1}.
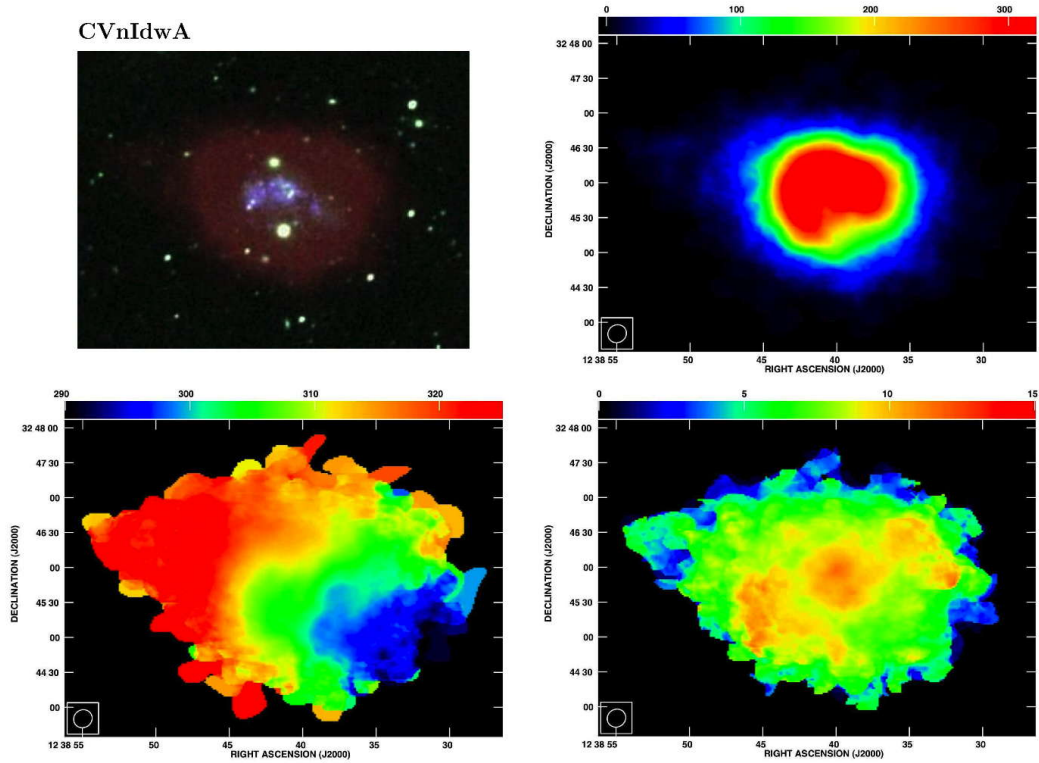
Fig. 12.— Basic data for CVnIdwA. H I data are made from the Hanning-smoothed Naturally-weighted cube. *Upper left:* False color picture combining H I (*red*), *V*-band (*green*), and FUV (*blue*). *Upper right:* Integrated H I. The color wedge is in units of Jy beam^{-1} m s^{-1}. *Bottom left:* Intensity-weighted velocity field. *Bottom right:* Intensity-weighted velocity dispersion. The color wedge for both bottom panels is in km s^{-1}.

Table 1. The Galaxy Sample

Galaxy	Other names [a]	D (Mpc)	Ref [b]	M_V (mag)	R_H [c] (arcmin)	R_D [c] (kpc)	$E(B-V)_f$ [d]	$\log \mathrm{SFR}_D^{H\alpha\,e}$ ($M_\odot$ yr^{-1} kpc^{-2})	$\log \mathrm{SFR}_D^{FUV\,e}$ ($M_\odot$ yr^{-1} kpc^{-2})	$12 + \log \mathrm{O/H}$ [f]	Ref [g]
					Im Galaxies						
CVnIdwA	UGCA 292	3.6	1	−12.4	0.87	0.57±0.12	0.01	−2.58±0.01	−2.48±0.01	7.3±0.06	24
DDO 43	PGC 21073, UGC 3860	7.8	2	−15.1	0.89	0.41±0.03	0.05	−1.78±0.01	−1.55±0.01	8.3±0.09	25
DDO 46	PGC 21585, UGC 3966	6.1	⋯	−14.7	⋯	1.14±0.06	0.05	−2.89±0.01	−2.46±0.01	8.1±0.1	25
DDO 47	PGC 21600, UGC 3974	5.2	3	−15.5	2.24	1.37±0.06	0.02	−2.70±0.01	−2.40±0.01	7.8±0.2	26
DDO 50	PGC 23324, UGC 4305, Holmberg II, VIIZw 223	3.4	1	−16.6	3.97	1.10±0.05	0.02	−1.67±0.01	−1.55±0.01	7.7±0.14	27
DDO 52	PGC 23769, UGC 4426	10.3	4	−15.4	1.08	1.30±0.13	0.03	−3.20±0.01	−2.43±0.01	(7.7)	28
DDO 53	PGC 24050, UGC 4459, VIIZw 238	3.6	1	−13.8	1.37	0.72±0.06	0.03	−2.42±0.01	−2.41±0.01	7.6±0.11	27
DDO 63	PGC 27605, Holmberg I, UGC 5139, Mailyan 044	3.9	1	−14.8	2.17	0.68±0.01	0.01	−2.32±0.01	−1.95±0.00	7.6±0.11	27
DDO 69	PGC 28868, UGC 5364, Leo A	0.8	5	−11.7	2.40	0.19±0.01	0.00	−2.83±0.01	−2.22±0.01	7.4±0.10	29
DDO 70	PGC 28913, UGC 5373, Sextans B	1.3	6	−14.1	3.71	0.48±0.01	0.01	−2.85±0.01	−2.16±0.00	7.5±0.06	30
DDO 75	PGC 29653, UGCA 205, Sextans A	1.3	7	−13.9	3.09	0.22±0.01	0.02	−1.28±0.01	−1.07±0.01	7.5±0.06	30
DDO 87	PGC 32405, UGC 5918, VIIZw 347	7.7	⋯	−15.0	1.15	1.31±0.12	0.00	−1.36±0.01	−1.00±0.01	7.8±0.04	31
DDO 101	PGC 37449, UGC 6900	6.4	⋯	−15.0	1.05	0.94±0.03	0.01	−2.85±0.01	−2.81±0.01	8.7±0.03	25
DDO 126	PGC 40791, UGC 7559	4.9	8	−14.9	1.76	0.87±0.03	0.00	−2.37±0.01	−2.10±0.01	(7.8)	28
DDO 133	PGC 41636, UGC 7698	3.5	⋯	−14.8	2.33	1.24±0.09	0.00	−2.88±0.01	−2.62±0.01	8.2±0.09	25
DDO 154	PGC 43869, UGC 8024, NGC 4789A	3.7	⋯	−14.2	1.55	0.59±0.03	0.01	−2.50±0.01	−1.93±0.01	7.5±0.09	27
DDO 155	PGC 44491, UGC 8091, GR 8, LSBC D646-07	2.2	9	−12.5	0.95	0.15±0.01	0.01	−1.44±0.01	⋯	7.7±0.06	29
DDO 165	PGC 45372, UGC 8201, IIZw 499, Mailyan 82	4.6	10	−15.6	2.14	2.26±0.08	0.01	−3.67±0.01	⋯	7.6±0.08	27
DDO 167	PGC 45939, UGC 8308	4.2	8	−13.0	0.75	0.33±0.05	0.00	−2.36±0.01	−1.83±0.01	7.7±0.2	26
DDO 168	PGC 46039, UGC 8320	4.3	8	−15.7	2.32	0.82±0.01	0.00	−2.27±0.01	−2.04±0.01	8.3±0.07	25
DDO 187	PGC 50961, UGC 9128	2.2	1	−12.7	1.06	0.18±0.01	0.00	−2.52±0.01	−1.98±0.01	7.7±0.09	32
DDO 210	PGC 65367, Aquarius Dwarf	0.9	10	−10.9	1.31	0.17±0.01	0.03	⋯	−2.71±0.06	(7.2)	28
DDO 216	PGC 71538, UGC 12613, Peg DIG, Pegasus Dwarf	1.1	11	−13.7	4.00	0.54±0.01	0.02	−4.10±0.07	−3.21±0.01	7.9±0.15	33
F564-V3	LSBC D564-08	8.7	4	−14.0	⋯	0.53±0.03	0.02	⋯	−2.79±0.02	(7.6)	28
IC 10	PGC 1305, UGC 192	0.7	12	−16.3	⋯	0.40±0.01	0.75	−1.11±0.01	⋯	8.2±0.12	34
IC 1613	PGC 3844, UGC 668, DDO 8	0.7	13	−14.6	9.10	0.58±0.02	0.00	−2.56±0.01	−1.99±0.01	7.6±0.05	35
LGS 3	PGC 3792, Pisces dwarf	0.7	14	−9.7	0.96	0.23±0.02	0.04	⋯	−3.88±0.06	(7.0)	28
M81dwA	PGC 23521	3.5	15	−11.7	⋯	0.26±0.00	0.02	⋯	−2.26±0.01	(7.3)	28
NGC 1569	PGC 15345, UGC 3056, Arp 210, VIIZw 16	3.4	16	−18.2	⋯	0.38±0.02	0.51	0.19±0.01	−0.01±0.05	8.2±0.05	36
NGC 2366	PGC 21102, UGC 3851, DDO 42	3.4	17	−16.8	4.72	1.36±0.04	0.04	−1.67±0.01	−1.66±0.01	7.9±0.01	37
NGC 3738	PGC 35856, UGC 6565, Arp 234	4.9	3	−17.1	2.40	0.78±0.01	0.00	−1.66±0.01	−1.53±0.01	8.4±0.01	25
NGC 4163	PGC 38881, NGC 4167, UGC 7199	2.9	1	−14.4	1.47	0.27±0.03	0.00	−2.28±0.13	−1.74±0.01	7.9±0.2	38
NGC 4214	PGC 39225, UGC 7278	3.0	1	−17.6	4.67	0.75±0.01	0.00	−1.03±0.01	−1.08±0.01	8.2±0.06	39
NGC 6822	PGC 63616, IC 4895, DDO 209, Barnard's Galaxy	0.5	18	−15.2	⋯	0.57±0.03	0.22	−2.06±0.01	−1.82±0.01	8.1±0.22	27
SagDIG	PGC 63287, Lowal's Object	1.1	19	−12.5	⋯	0.23±0.03	0.14	−2.97±0.04	−2.11±0.01	7.3±0.1	35
UGC 8508	PGC 47495, IZw 60	2.6	1	−13.6	1.28	0.27±0.01	0.00	−2.03±0.01	⋯	7.9±0.2	38
WLM	PGC 143, UGCA 444, DDO 221, Wolf-Lundmark-Melott	1.0	20	−14.4	5.81	0.57±0.03	0.02	−2.77±0.01	−2.05±0.01	7.8±0.06	40
					BCD Galaxies						
Haro 29	PGC 40665, UGCA 281, Mrk 209, I Zw 36	5.8	21	−14.6	0.84	0.29±0.01	0.00	−0.77±0.01	−1.07±0.01	7.9±0.07	41
Haro 36	PGC 43124, UGC 7950	9.3	⋯	−15.9	⋯	0.69±0.01	0.00	−1.86±0.01	−1.55±0.01	8.4±0.08	25
Mrk 178	PGC 35684, UGC 6541	3.9	8	−14.1	1.01	0.33±0.01	0.00	−1.60±0.01	−1.66±0.01	7.7±0.02	42
VIIZw 403	PGC 35286, UGC 6456	4.4	22,23	−14.3	1.11	0.52±0.02	0.02	−1.71±0.01	−1.67±0.01	7.7±0.01	25

[a] Selected alternate identifications obtained from NED.

[b] Reference for the distance to the galaxy. If no reference is given, the distance was determined from the galaxy's radial velocity, given by de Vaucouleurs et al. (1991), corrected for infall to the Virgo Cluster (Mould et al. 2000) and a Hubble constant of 73 km s^{-1} Mpc^{-1}.

[c] R_H is the Holmberg radius, the radius of the galaxy at a B-band isophote, corrected for reddening, of 26.7 mag of one arcsec^2. R_D is the disk scale length measured from V-band images. From Hunter & Elmegreen (2006).

[d] Foreground reddening from Burstein & Heiles (1984).

[e] $\mathrm{SFR}_D^{H\alpha}$ is the star formation rate, measured from Hα, normalized to the area πR_D^2, where R_D is the disk scale length (Hunter & Elmegreen 2004). SFR_D^{FUV} is the star formation rate determined from $GALEX$ FUV fluxes (Hunter et al. 2010, with an update of the $GALEX$ FUV photometry to the GR4/GR5 pipeline reduction).

[f] Values in parentheses were determined from the empirical relationship between oxygen abundance and M_B given by Richer & McCall (1995) and are particularly uncertain.

[g] Reference for the oxygen abundance.

References. — (1) Dalcanton et al. 2009; (2) Karachentsev et al. 2004; (3) Karachentsev et al. 2003a; (4) Karachentsev et al. 2006; (5) Dolphin et al. 2002; (6) Sakai et al. 2004; (7) Dolphin et al. 2003; (8) Karachentsev et al. 2003b; (9) Tolstoy et al. 1995a; (10) Karachentsev et al. 2002; (11) Meschin et al. 2009; (12) Sakai et al. 1999; (13) Pietrzynski et al. 2006; (14) Miller et al. 2001; (15) Freedman et al. 2001;

16) Grocholski et al. 2008; (17) Tolstoy et al. 1995b; (18) Gieren et al. 2006; (19) Momany et al. 2002; (20) Gieren et al. 2008; (21) Schulte-Ladbeck et al. 2001; (22) Lynds et al. 1998; (23) Méndez et al. 2002; 24) van Zee & Haynes 2006; (25) Hunter & Hoffman 1999; (26) Skillman, Kennicutt, & Hodge 1989; (27) Moustakas et al. 2010; (28) Richer & McCall 1995; (29) van Zee et al. 2006; (30) Kniazev et al. 2005; (31) Croxall et al. 2009; (32) Lee et al. 2003b; (33) Skillman et al. 1997; (34) Lequex et al. 1979; (35) Lee et al. 2003a; (36) Kobulnicky & Skillman 1997; (37) González-Delgado et al. 1994; (38) Moustakas & Kennicutt 2006); (39) Masegosa et al. 1991; (40) Lee et al. 2005; (41) Viallefond & Thuan 1983; (42) González-Riestra et al. 1988.

Table 2. The Data Sets

Data set	No. Galaxies	Purpose	Status
VLA HI-line maps[a]		Trace cloud formation	
Archives (1.3 km s^{-1})	9		This paper
(2.6 km s^{-1})	11		This paper
New Obs (1.3 km s^{-1})	11		This paper
(2.6 km s^{-1})	10		This paper
Hα images	41	Trace current star formation	Hunter & Elmegreen (2004)
GALEX UV		Trace recent star formation	
Archives	27		Hunter et al. (2010), Herrmann et al. (2012)
New	11		Zhang et al. (2012b), Herrmann et al. (2012)
UBV images	41	Trace star formation over past Gyr	Hunter & Elmegreen (2006), Herrmann et al. (2012)
JHK images J	8	Trace star formation over galaxy lifetime	Hunter & Elmegreen (2006), Herrmann et al. (2012)
JH	3		
JHK	6		
Spitzer IRAC images	36	Trace stars, hot dust, PAHs	Hunter et al. (2006), Herrmann et al. (2012)
Spitzer MIPS images	35	Trace embedded star formation, dust	Archives
Molecular clouds		Star-forming clouds	
CARMA - CO obs	1		Data reduced
APEX - CO obs	1		Data reduced; additional observations in progress
Herschel - PDRs	5		Observations in progress
Dust		ISM heating balance	
APEX - FIR	3		Data reduced for one galaxy; additional observations in progress
Herschel - FIR	5		Observations in progress

[a]1.3 km s^{-1} and 2.6 km s^{-1} refer to the channel separation.

Table 3. The VLA Observations

Galaxy	Array	Obs Dates[a]	Project ID[b]	TOS[c] (hr)	Ch sep (km s^{-1})	Final # Ch	ROBUST-weighted map cube Beam[d] (arcs×arcs)	Beam PA (deg)	RMS (mJy bm^{-1})	Natural-weighted map cube Beam[d] (arcs×arcs)	Beam PA (deg)	RMS (mJy bm^{-1})
Im Galaxies												
CVnIdwA	B	07 Dec 3, 08 Feb 6	AO215,AH927	8.3	1.3	101	10.9×10.5	82.0	0.65	16.3×15.1	-57.7	0.58
	CnB	08 Feb 7	AH927	0.9								
	C	99 Jan 24, 08 Jul 11	AL471,AO215	6.5								
	D	08 Jul 11, 08 Jul 31, 08 Aug 16	AO215,AH927	2.6								
DDO 43	B	08 Jan 13, 08 Jan 22, 08 Jan 26	AH927	10.9	2.6	106	8.1×6.0	88.5	0.55	14.3×12.3	-79.7	0.50
	C	93 Jul 5, 00 Apr 9	AS506,AH695	4.6								
	D	96 Sep 20, 01 Oct 19	AS591,AH753	2.9								
DDO 46	B	07 Dec 19,08 Jan 6,08 Jan 15,08 Jan 16	AH927	12.2	2.6	102	6.3×5.2	81.5	0.57	9.8×7.1	73.9	0.52
	C	08 Mar 18, 08 Mar 22, 08 Apr 2	AH927	5.2								
	D	08 Jul 6, 08 Jul 26	AH927	1.5								
DDO 47	AB	91 Dec 27	AP216	6.3	2.6	107	10.4×9.0	76.2	0.68	16.1×15.3	63.4	0.61
	C	92 May 3	AP216	3.7								
	CD	91 Feb 10	TEST02	3.1								
	D	91 Apr 16	AC284	2.0								
DDO 50	B	90 Aug 10	AP196	5.1	2.6	108	7.0×6.1	-32.9	1.07	13.7×12.6	-40.1	1.02
	C	90 Dec 2	AP196	2.0								
	D	91 Mar 7	AP196	1.7								
DDO 52	B	08 Jan 5, 08 Jan 8, 08 Jan 21	AH927	10.8	2.6	104	6.8×5.2	65.9	0.55	11.8×7.2	72.9	0.51
	CnB	08 Feb 8	AH927	4.5								
	C	08 Mar 30, 08 Apr 4	AH927	5.8								
	D	08 Jul 25	AH927	1.9								
DDO 53	B	03 Dec 22	AW605	5.7	2.6	108	6.3×5.7	2.6	0.60	11.8×9.5	-6.0	0.56
	C	04 Feb 23	AW605	0.5								
	D	04 Jul 9	AW605	1.4								
DDO 63	B	90 Jul 23	AP196	5.7	2.6	108	7.8×6.0	-71.5	1.19	14.7×12.7	-41.6	1.06
	C	90 Dec 2	AP196	2.0								
	D	91 Mar 7	AP196	1.7								
DDO 69	B	95 Dec 2	AY072	7.2	1.3	107	5.8×5.4	89.3	0.66	8.3×7.7	70.8	0.62
	C	92 Apr 20	AL258	5.6								
	D	92 Jul 19	AL258	1.8								
DDO 70	B	05 May 7, 05 May 8, 07 Nov 16	AH866,AO215	4.9	1.3	107	13.8×13.2	-56.6	0.70	17.9×17.5	-11.5	0.62
	C	97 Aug 2	AM561	5.1								
	D	01 Dec 6	AH753	3.3								
DDO 75	AB	94 Jun 17	TEST	0.7	2.6	104	7.6×6.5	13.7	0.51	11.9×10.0	4.2	0.45
	B	05 May 9, 05 May 10, 07 Nov 21	AH866,AO215	5.1								
	C	92 May 9, 04 May 14, 08 Mar 16	TEST,AH836,AO215	9.1								
	D	92 Jul 13	TEST	1.5								
DDO 87	B	08 Jan 29, 08 Feb 2, 08 Feb 3	AH927	10.8	2.6	104	7.6×6.2	61.3	0.54	12.8×11.9	63.1	0.51
	C	97 Sep 8	AH608	3.7								
	D	08 Jul 20, 08 Aug 5	AH927	1.7								
DDO 101	B	08 Jan 8, 08 Jan 16, 08 Feb 4	AH927	7.2	2.6	101	8.3×7.0	64.4	0.58	12.6×12.5	46.8	0.52
	CnB	08 Feb 9, 08 Feb 10	AH927	2.4								
	C	06 Dec 16	AH918	3.8								
	D	08 Jul 25	AH927	2.0								
DDO 126	B	08 Jan 14, 08 Jan 18, 08 Jan 26	AH927	9.8	1.3	102	6.9×5.6	61.1	0.46	12.2×9.3	75.7	0.43
	C	08 Mar 17	AH927	4.6								

Table 3—Continued

Galaxy	Array	Obs Dates[a]	Project ID[b]	TOS[c] (hr)	Ch sep ($\mathrm{km\,s^{-1}}$)	Final # Ch	ROBUST Beam[d] (arcs×arcs)	ROBUST Beam PA (deg)	ROBUST RMS ($\mathrm{mJy\,bm^{-1}}$)	Natural Beam[d] (arcs×arcs)	Natural Beam PA (deg)	Natural RMS ($\mathrm{mJy\,bm^{-1}}$)
DDO 133	DnC	08 Jun 11	AH927	1.3								
	D	08 Jul 6, 08 Jul 19	AH927	1.7								
	B	07 Dec 24, 08 Jan 7, 08 Jan 11, 08 Feb 2	AH927	12.9	2.6	102	12.4×10.8	-87.9	0.37	19.2×18.1	-84.0	0.33
	C	08 Mar 22, 08 Jun 3	AH927	6.0								
	D	04 Jun 21, 04 Aug 21	AH843	8.2								
DDO 154	B	05 May 6	AW605	6.3	2.6	108	7.9×6.3	-87.2	0.54	14.1×12.6	-58.1	0.52
	C	04 Apr 28	AW605	1.7								
	D	04 Jul 5	AW605	1.5								
DDO 155	B	07 Nov 12	AO215	8.1	1.3	95	11.3×10.1	-84.6	0.65	16.2×15.2	-52.9	0.60
	CnB	08 Feb 10, 08 Feb 10	AH927	2.0								
	C	99 Jan 25, 08 Jul 13	AL471	6.3								
	D	08 Jul 13, 08 Aug 2, 08 Aug 2, 08 Aug 17	AO215,AH927	6.3	2.8							
DDO 165	B	08 Jan 25, 08 Feb 3	AH927	9.4	1.3	101	10.0×7.6	67.1	0.64	14.8×12.9	78.1	0.62
	CnB	08 Feb 9	AH927	1.7								
	C	08 Mar 23, 08 Apr 14	AH927	5.8								
	D	08 Jul 7, 08 Jul 31	AH927	1.7								
DDO 167	B	08 Jan 24, 08 Jan 27, 08 Jan 29	AH927	10.1	1.3	101	7.3×5.3	63.2	0.72	12.2×7.0	54.4	0.66
	CnB	08 Feb 8	AH927	4.6								
	C	08 Mar 19, 08 May 29	AH927	5.1								
	D	08 Jul 25	AH927	1.9								
DDO 168	B	08 Jan 20, 08 Feb 1, 08 Feb 6	AH927	10.3	2.6	103	7.8×5.8	67.5	0.51	12.6×11.2	63.2	0.47
	C	08 Mar 27, 08 Apr 22	AH927	6.0								
	D	08 Jul 7	AO215	2.0								
DDO 187	B	07 Nov 17	AO215	7.9	1.3	99	6.2×5.5	62.9	0.62	12.4×11.0	-88.8	0.54
	CnB	08 Feb 10, 08 Feb 12	AH927	1.8								
	C	08 Mar 28, 08 May 30	AO215,AH927	3.8								
	D	08 Jul 11, 08 Aug 5, 08 Aug 6, 08 Aug 16	AO215,AH927	3.1								
DDO 210	B	02 Aug 2, 02 Aug 9, 02 Aug 19	AH752	6.6	1.3	107	11.7×8.6	-6.78	0.87	16.6×14.1	-4.0	0.80
	C	99 Jan 25	AL471	5.6								
	CD	95 Jan 20	AL349	2.1								
	D	02 Nov 1	AH752	3.1								
DDO 216	C	99 Jan 24	AL471	5.5	1.3	107	16.2×15.4	69.8	0.96	20.0×18.9	55.2	0.88
	D	95 Mar 13	AL349	2.0								
F564-V3	B	08 Jan 8, 08 Jan 25, 08 Jan 28	AH927	9.7	1.3	103	12.5×8.1	70.7	0.69	17.5×16.0	64.5	0.63
	C	02 Dec 15	AH752	3.2								
	D	01 Dec 10	AH752	3.3								
IC 10	A	04 Sep 22, 04 Sep 24, 04 Sep 28	AW643	22.7	2.6	107	5.9×5.5	16.1	0.48	8.4×7.4	37.4	0.46
	B	94 Aug 24, 94 Aug 30	AW383	11.2								
	C	93 Aug 17	AW359	5.8								
	D	94 Feb 6	AW359	0.1								
IC 1613	B	95 Dec 16, 95 Dec 18	AW404	12.1	2.6	107	7.7×6.5	6.7	0.40	13.2×11.0	-5.0	0.37
	C	96 Feb 11	AW404	5.9								
	D	95 Apr 14	AW404	3.6								
LGS 3	B	08 Jan 5	AH927	4.7	1.3	84	11.8×9.3	61.6	0.93	17.4×16.8	78.6	0.75
	C	94 Nov 12	AY066	4.5								
M81dwA	B	95 Apr 2, 03 Apr 18, 03 Apr 22, 03 Apr 26	AY066,AR510	3.7	1.3	108	7.8×6.3	4.5	0.84	15.9×14.2	10.2	0.74
	B	03 Dec 16	AW605	6.2								
	C	02 Nov 3, 02 Dec 15	AT285,AH752	5.5								
	D	01 Dec 10	AH752	3.2								

Table 3—Continued

Galaxy	Array	Obs Dates[a]	Project ID[b]	TOS[c] (hr)	Ch sep (km s^{-1})	Final # Ch	ROBUST-weighted map cube			Natural-weighted map cube		
							Beam[d] (arcs×arcs)	Beam PA (deg)	RMS (mJy bm^{-1})	Beam[d] (arcs×arcs)	Beam PA (deg)	RMS (mJy bm^{-1})
NGC 1569	B	03 Nov 10	AW605	6.0	2.6	107	5.9×5.2	21.9	0.60	7.7×7.0	16.5	0.55
	C	93 Jun 29	AW325	5.1								
	D	92 Sep 6	AW325	2.5								
NGC 2366	B	03 Dec 3	AW605	5.4	2.6	108	6.9×5.9	20.1	0.63	13.0×11.8	-1.6	0.61
	BC	04 Feb 23	AW605	0.5								
	D	04 Jul 2	AW605	1.4								
NGC 3738	B	08 Jan 22, 08 Feb 1, 08 Feb 6	AH927	10.9	2.6	102	6.3×5.5	70.6	0.50	13.0×7.8	84.8	0.46
	C	08 Apr 1, 08 May 31	AH927	5.2								
	D	08 Jul 20, 08 Jul 29	AH927	1.7								
NGC 4163	B	07 Nov 23	AO215	7.2	2.6	95	9.7×5.9	-86.4	0.73	21.3×20.1	-81.8	0.52
	CnB	08 Feb 12, 08 Feb 12	AH927	1.9								
	C	08 Apr 8, 08 Jun 1	AH927	3.6								
	D	04 Jun 20, 04 Aug 21, 08 Aug 6	AO215,AH843	8.2								
NGC 4214	B	94 Jun 30, 94 Jul 1	AM418	6.0	1.3	108	7.6×6.4	89.8	0.73	14.7×13.9	-48.2	0.66
	C	93 Aug 9	AM418	3.9								
	D	94 Jan 27	AM418	2.2								
NGC 6822	B	08 Jan 14, 08 Jan 19, 08 Jan 25	AH927	10.5	1.3	...	...	...	...	...	...	...
	BC	93 Jun 5	AW312	5.5								
	C	08 Mar 27, 08 Apr 27	AH927	5.7								
	D	92 Sep 7, 08 Jul 14, 08 Jul 24	AW312,AH927	7.9								
SagDIG	C	92 Apr 21	AL258	5.4	1.3	107	28.2×16.9	-4.1	2.05	39.8×24.4	-6.4	2.20
	D	92 Jul 16	AL258	2.1								
UGC 8508	B	07 Dec 10	AO215	1.3	1.3	102	5.9×4.9	-88.7	0.99	9.5×5.9	-85.8	0.91
	CnB	08 Feb 9, 08 Feb 9	AH927	1.8								
	C	08 Mar 15, 08 May 31	AO215,AH927	3.5								
	D	08 Jul 13, 08 Jul 31, 08 Aug 3	AO215,AH927	2.7								
WLM	B	02 Jul 9, 02 Jul 12	AH753	8.4	2.6	107	7.6×5.1	-3.4	0.82	10.6×7.4	-14.2	0.76
	C	00 Mar 31	AH695	5.2								
	D	01 Oct 19	AH753	0.33								
BCD Galaxies												
Haro 29	B	08 Jan 28, 08 Jan 30	AH927	9.2	1.3	103	6.8×5.6	59.3	0.52	12.4×7.9	69.7	0.48
	CnB	08 Feb 7	AH927	1.7								
	C	08 Mar 23, 08 Apr 19	AH927	5.9								
	D	08 Jul 6, 08 Jul 29	AH927	1.7								
Haro 36	B	08 Jan 15, 08 Jan 21, 08 Jan 27	AH927	10.3	2.6	106	7.0×5.8	62.6	0.53	12.4×8.9	66.2	0.49
	C	08 Mar 23, 08 Apr 15	AH927	5.7								
	D	08 Jul 8, 08 Jul 24, 08 Jul 25	AH927	2.2								
Mrk 178	B	08 Jan 17, 08 Jan 20, 08 Jan 26	AH927	10.4	1.3	105	6.2×5.5	71.6	0.69	12.0×7.5	80.3	0.64
	C	08 Mar 19, 08 Apr 27	AH927	5.7								
	D	08 Jul 20, 08 Jul 30	AH927	1.7								
VIIZw 403	B	06 Sep 10	AH907	8.6	2.6	107	9.4×7.7	81.7	0.71	17.8×17.6	1.3	0.60
	C	92 Apr 11	AH453	3.7								
	D	97 Nov 10	AH623	4.0								

[a]Date when the observations began.

Table 4.   Integrated Masses

Galaxy	Conversion Factor[a] $(M_\odot (\text{Jy beam}^{-1} \text{ m s}^{-1})^{-1})$	$\log S_\nu$[b] $(\text{Jy beam}^{-1} \text{ m s}^{-1})$	$\log M_{HI}$ $(M_\odot)$
	Im Galaxies		
CVnIdwA	52.98	5.95	7.67
DDO 43	595.15	5.45	8.23
DDO 46	530.30	5.55	8.27
DDO 47	134.65	6.46	8.59
DDO 50	125.49	6.75	8.85
DDO 52	1404.03	5.28	8.43
DDO 53	169.40	5.49	7.72
DDO 63	152.10	6.01	8.19
DDO 69	9.66	5.86	6.84
DDO 70	4.35	6.97	7.61
DDO 75	16.28	6.65	7.86
DDO 87	592.62	5.62	8.39
DDO 101	331.75	4.84	7.36
DDO 126	293.50	5.69	8.16
DDO 133	43.13	6.39	8.02
DDO 154	129.01	6.35	8.46
DDO 155	19.85	5.70	7.00
DDO 165	131.87	6.01	8.13
DDO 167	215.81	4.84	7.17
DDO 168	191.09	6.17	8.47
DDO 187	66.04	5.30	7.12
DDO 210	3.79	5.72	6.30
DDO 216	12.41	5.65	6.75
F564V3	351.11	5.07	7.61
IC 10	7.08	6.93	7.78
IC 1613	4.61	6.86	7.53
LGS3	2.09	4.87	5.19
M81dwA	124.28	5.09	7.18
NGC 1569	179.04	6.14	8.39

Table 4—Continued

Galaxy	Conversion Factor[a] $(M_\odot(\text{Jy beam}^{-1}\text{ m s}^{-1})^{-1})$	$\log S_\nu$[b] $(\text{Jy beam}^{-1}\text{ m s}^{-1})$	$\log M_{HI}$ $(M_\odot)$
NGC 2366	132.41	6.72	8.84
NGC 3738	326.55	5.54	8.06
NGC 4163	69.27	5.32	7.16
NGC 4214	87.28	6.82	8.76
Sag DIG	6.47	6.13	6.94
UGC 8508	109.21	5.24	7.28
WLM	12.21	6.76	7.85
BCD Galaxies			
Haro 29	416.32	5.18	7.80
Haro 36	1010.34	5.15	8.16
Mrk 178	210.35	4.67	6.99
VIIZw 403	125.27	5.59	7.69

[a]Factor to convert flux in the ROBUST-weighted integrated H I map to mass in solar masses. Note this conversion factor contains the necessary division by the number of pixels per beam, as discussed in §4.

[b]Integrated flux measured on the integrated H I map made from the ROBUST-weighted image cube.

Table 5.   Velocity Profiles and Single-dish comparison

Galaxy	Instrument	Ref	Comments
			Im Galaxies
CVnIdwA	Green Bank 42m	13	Excellent agreement.
DDO 43	Green Bank 91m	13	Profiles match very well, with the VLA only missing a small part of single-dish emission near the center.
DDO 46	Green Bank 91m	8,13	Profiles match quite well, with only minimal difference in the center.
DDO 47	Green Bank 42m	13	Excellent agreement.
DDO 50	Green Bank 91m	9	The shapes are roughly the same, but the single dish picks up more emission on the high velocity side. This could result from gas with low surface brightness.
DDO 52	Green Bank 42m	13	Excellent agreement.
DDO 53	Effelsberg 100m	5	Only a partial single-dish spectrum available, due to Galactic confusion. The VLA profile matches the available data quite well.
DDO 63	Effelsberg 100m	13	Good agreement, with the VLA recovering 10% less emission at the peak. This falls within the measurement uncertainty.
DDO 69	Green Bank 42m	8,15	The VLA recovers about 30% less flux than the single dish. There is significant Galactic HI emission below 0 km/s.
DDO 70	Green Bank 42m	15	Excellent agreement.
DDO 75	Green Bank 42m	13	Excellent agreement.
DDO 87	Green Bank 42m	6	While the profiles are similar for the most part, the VLA does not recover the horns visible in the single-dish data. These may not be real, as the horns are roughly the same size as the noise seen to the side of the profile.
DDO 101	Arecibo	10	The profiles roughly agree, though the VLA in general recovers more flux.
DDO 126	Effelsberg 100m	4	The two instruments show slightly different distributions of gas in velocity space, likely due to surface brightness. Flux levels roughly match, except for a slight excess in the single-dish profile on the high-velocity side.
DDO 133	Green Bank 42m	13	Very good agreement.
DDO 154	Green Bank 42m	13	The general shapes are very similar, however the VLA recovers more than twice the flux as the 42m, and recovers some lower-velocity emission near the peak missed with Effelsberg. This arises because the Effelsberg HPBW is smaller than the galaxy on the sky.
DDO 155	Arecibo	1	Good agreement.
DDO 165	Effelsberg 100m	5	The profiles match up well on the low-velocity side, but there is a significant single-dish excess on the high velocity side. This is likely due to surface brightness sensitivity.
DDO 167	Effelsberg 100m	5	There is generally good agreement, though the VLA levels are roughly 10% less than the single-dish. This falls within the measurement uncertainty.
DDO 168	Effelsberg 42m	6	The VLA picks up slightly more emission at the slow side of the peak, but slightly less through the rest of the peak.
DDO 187	Green Bank 42m	13	The profiles agree, but the VLA peak is 20% lower than the single-dish. Taking into account the single-dish noise level and measurement uncertainty, the levels agree.
DDO 210	Nancay	13	Excellent agreement, though the VLA misses some faint extended emission around -100km/s.
DDO 216	Effelsberg 100m	5	The profile shapes match, with the VLA recovering slightly more flux at the peak.
F564-V3	Arecibo	2	The overall agreement is fair, though the noise level can account for most differences. The Arecibo power beam is roughly the size of the galaxy, giving the VLA an edge in recovering flux, as we see.
IC 10	Dwingeloo 25m	12	The VLA misses much of the emission seen in the single-dish profile. The galaxy is almost as large on the sky as the HPBW of each instrument, thus the inherent surface brightness sensitivity advantage of the single-dish telescope will result in the capture of more flux overall.
IC 1613	Green Bank 91m	9	The overall profiles agree, but the VLA flux is roughly 1/3 lower than the single-dish measurement. This is likely due to surface brightness sensitivity compounded over the galaxy's large area.
LGS3	Effelsberg 100m	5	The agreement is good, especially considering the noise level.
M81 dwA	Effelsberg 100m	5	Good agreement.
NGC 1569	Green Bank 91m	11	The profiles differ greatly at high velocities, mostly due to significant Galactic HI confusion around -50 km/s. This galaxy is also relatively large on the sky, which can result in some mismatch between the data sets.
NGC 2366	Green Bank 91m	14	While the VLA recovers more flux overall, it shows additional HI structure in the high-velocity part of the profile, above the levels of the single-dish measurement. This is a result of the single-dish HPBW missing some extended emission from only being roughly the size of the galaxy.
NGC 3738	Effelsberg 100m	4	The profiles agree reasonably well.
NGC 4163	Effelsberg 100m	4	The profiles agree until just before the peak. There is some VLA excess right around the peak, but the high-velocity side has significant single-dish excess, likely due to surface brightness sensitivity.
NGC 4214	Effelsberg 100m	3	The Effelsberg profile recovers more flux from the low-velocity side through the peak. This galaxy is relatively large on the sky, which may account for some mismatch between the two data sets.
Sag DIG	Green Bank 42m	15	The profiles match very well. There is a significant excess in the Green Bank data starting at -40 km/s, which is due to Galactic HI emission.
UGC 8508	Effelsberg 100m	4	The profiles match reasonably well, though the VLA recovers roughly 1/3 less flux near the peak. This could be due to the relatively high noise in this small galaxy.
WLM	Parkes	7	Good agreement, with some VLA excess at the peak and low-velocity side of the profile. This is due to the Parkes HPBW being smaller than the galaxy on the sky.
			BCD Galaxies
Haro 29	Green Bank 91m	14	The profiles show good agreement, but there is a wing of slight single-dish excess of very low brightness on the low-velocity side.
Haro 36	Green Bank 91m	14	The profiles show good agreement, even through the single-dish noise.
Mrk 178	Green Bank 91m	14	The profiles are roughly the same shape, though the VLA picks up 25% more flux at the peak, and the single-dish measurement shows some extended emission that the VLA misses.
VII Zw 403	Green Bank 91m	14	The profiles generally agree quite well, aside from a large single-dish spike of Galactic cirrus.

References. — (1) Giovanelli et al. 2007, (2) Eder & Schombert 2000, (3) Huchtmeier & Seiradakis 1985, (4) Huchtmeier & Richter 1986, (5) Huchtmeier et al. 2003, (6) Hunter & Gallagher 1985, (7) Koribalski et al. 2004, (8) Lewis, Helou, Salpeter 1985, (9) Rots 1980, (10) Schneider et al. 1990, (11) Schneider et al. 1992, (12) Shostak & Allen 1980, (13) Springob et al. 2005, (14) Thuan & Martin 1981, (15) Young & Lo 1997. DDO 69 and DDO 70 show data that was previously unpublished, but taken by Young and processed in the same manner as the published SagDIG data.

Table 6.   Surface Density Photometry Parameters[a]

Galaxy	R.A. (2000.0) (hh mm ss.s)	Decl. (2000.0) (dd mm ss)	P.A.[b] (deg)	b/a[c]	Incl (deg)
		Im Galaxies			
CVnIdwA	12 38 40.2	+32 45 40	80	0.78	41.0
DDO 43	7 28 17.8	+40 46 13	6.5	0.70	48.5
DDO 46	7 41 26.6	+40 06 39	84	0.89	28.6
DDO 47	7 41 55.3	+16 48 08	-70	0.51	64.4
DDO 50	8 19 08.7	+70 43 25	18	0.72	46.7
DDO 52	8 28 28.5	+41 51 21	5	0.67	51.1
DDO 53	8 34 08.0	+66 10 37	81	0.51	64.4
DDO 63	9 40 30.4	+71 11 02	0	1.00	0.0
DDO 69	9 59 25.0	+30 44 42	-64	0.56	60.3
DDO 70	10 00 00.9	+ 5 19 50	88	0.59	57.8
DDO 75	10 10 59.2	-04 41 56	41	0.85	33.5
DDO 87	10 49 34.7	+65 31 46	76.5	0.58	58.6
DDO 101	11 55 39.4	+31 31 08	-69	0.69	49.4
DDO 126	12 27 06.5	+37 08 23	-41	0.47	67.7
DDO 133	12 32 55.4	+31 32 14	-6	0.69	49.4
DDO 154	12 54 06.2	+27 09 02	46	0.50	65.2
DDO 155	12 58 39.8	+14 13 10	51	0.71	47.6
DDO 165	13 06 25.3	+67 42 25	89	0.54	61.9
DDO 167	13 13 22.9	+46 19 11	-23	0.65	52.8
DDO 168	13 14 27.2	+45 55 46	-24.5	0.63	54.5
DDO 187	14 15 56.7	+23 03 19	37	0.80	39.0
DDO 210	20 46 52.0	-12 50 51	-85	0.48	66.9
DDO 216	23 28 35.0	+14 44 30	-58	0.45	69.4
F564-V3	9 02 53.9	+20 04 29	8.5	0.83	35.8
IC 10	0 20 21.9	+59 17 39	-38	0.78	41.0
IC 1613	1 04 49.2	+2 07 48	71	0.81	37.9
LGS 3	1 03 55.2	+21 52 39	-3.5	0.51	64.4
M81dwA	8 23 57.2	+71 01 51	86	0.73	45.8
NGC 1569	4 30 49.8	+64 50 51	-59	0.55	61.1

Table 6—Continued

Galaxy	R.A. (2000.0) (hh mm ss.s)	Decl. (2000.0) (dd mm ss)	P.A.[b] (deg)	b/a[c]	Incl (deg)
NGC 2366	7 28 48.8	+69 12 22	32.5	0.42	72.1
NGC 3738	11 35 49.0	+54 31 23	0	1.00	0.0
NGC 4163	12 12 09.2	+36 10 13	18	0.64	53.7
NGC 4214	12 15 39.2	+36 19 38	16	0.91	25.8
SagDIG	19 30 00.6	-17 40 56	87.5	0.53	62.7
UGC 8508	13 30 44.9	+54 54 29	-60	0.54	61.9
WLM	0 01 59.2	-15 27 41	-2	0.44	70.3
		BCD Galaxies			
Haro 29	12 26 16.7	+48 29 38	86	0.58	58.6
Haro 36	12 46 56.3	+51 36 48	2	0.81	37.9
Mrk 178	11 33 29.0	+49 14 24	-50	0.46	68.6
VIIZw 403	11 27 58.2	+78 59 39	-10	0.49	66.0

[a]From the V-band (Hunter & Elmegreen 2006).

[b]Position Angle (P.A.).

[c]Minor-to-major axis ratio as measured in an outer V-band surface brightness isophote. For computing the inclination of the galaxy, the intrinsic b/a is assumed to be 0.3 for dwarf galaxies (Hodge & Hitchcock 1966, van den Bergh 1988).